Assessing the lifetime of anthropogenic CO_2 and its sensitivity to different carbon cycle processes

Christine Kaufhold[1,2], Matteo Willeit[1], Bo Liu[3,4], and Andrey Ganopolski[1]

[1]Department of Earth System Analysis, Potsdam Institute for Climate Impact Research (PIK), Member of the Leibniz Association, P.O. Box 601203, D-14412 Potsdam, Germany
[2]Institute of Physics and Astronomy, Universität Potsdam, Potsdam, Germany
[3]Universität Hamburg, Hamburg, Germany
[4]Max Planck Institute for Meteorology, Hamburg, Germany

Correspondence: Christine Kaufhold (kaufhold@pik-potsdam.de)

Abstract. Although it is well-established that anthropogenic CO_2 emitted into the atmosphere will persist for a long time, the duration of the anthropogenic climate perturbation will depend on how rapidly the excess CO_2 is removed from the climate system by different biogeochemical processes. The uncertainty around the long-term climate evolution is therefore not only linked to the future of anthropogenic CO_2 emissions, but to our insufficient understanding of the long-term carbon cycle. Here, we use the fast Earth system model CLIMBER-X, which features a comprehensive carbon cycle, to examine the lifetime of anthropogenic CO_2 and its effects on the long-term evolution of atmospheric CO_2 concentration. This is done through an ensemble of 100,000 year long simulations, each driven by idealized CO_2 emission pulses. Our findings indicate that, depending on the magnitude of the emission, 75% of anthropogenic CO_2 is removed within 197–1,820 years after peak CO_2 concentration (with larger cumulative emissions taking longer to remove). Approximately 4.3% of anthropogenic CO_2 will remain beyond 100 kyr. We find that the uptake of carbon by land, which has only been marginally considered in previous studies, has a significant long-term effect, storing approximately 4–13% of anthropogenic carbon by the end of the simulation. Higher emission scenarios fall on the lower end of this range as increased soil respiration leads to greater carbon loss. For the first time, we have quantified the effect of dynamically changing methane concentrations on the long-term carbon cycle, showing that its effects are likely negligible over long timescales. The timescale of carbon removal via silicate weathering is also reassessed here, providing an estimate (80–105 kyrs) that is significantly shorter than some previous studies due to higher climate sensitivity, stronger weathering feedbacks, and the use of a spatially explicit weathering scheme, leading to a faster removal of anthropogenic CO_2 in the long-term. Furthermore, this timescale is shown to have a non-monotonic relationship with cumulative emissions. Our study highlights the importance of adding model complexity to the global carbon cycle in Earth system models, as to accurately represent the long-term future evolution of atmospheric CO_2.

1 Introduction

A large amount of research has been dedicated to studying the impact of anthropogenic CO_2 emissions on the climate, what oceanographer Roger Revelle coined as "man's great geophysical experiment" (Revelle, 1956; Revelle et al., 1965). The scope

of such research is usually limited to centennial timescales due to their relevance for governance and policy. However, there is a growing societal need and an increasing number of scientific inquiries on the long-term future. This particularly concerns the site selection for nuclear waste disposal and post-closure safety assessments of deep geological repositories, as a number of environmental factors, such as subterranean stress, permafrost, erosion, and subrosion, can potentially compromise long-term safety (Näslund et al., 2013; Lord et al., 2015a; Lindborg et al., 2018; Turner et al., 2023; Kurgyis et al., 2024).

Previous studies on long-term future climate evolution have primarily focused on one of two, tightly related research areas. Some, for example, have investigated the length of the current interglacial under natural conditions: Berger and Loutre (2002) showed that we were already positioned to experience an unusually prolonged interglacial period as we currently approach a minima in the 100-kyr and 400-kyr eccentricity cycle. A second area of interest is the lifetime of anthropogenic CO_2 in the atmosphere[1]: Archer et al. (1997) and Archer et al. (1998) improved previous estimates by including $CaCO_3$ dissolution kinetics, and showed that the return of atmospheric CO_2 concentration to pre-industrial conditions would take tens of thousands of years. These two overarching areas of focus converged in Archer (2005) and Archer and Ganopolski (2005), where they showed that, (1) not only is anthropogenic CO_2 expected to survive in our atmosphere for several hundreds of thousands of years, but (2) it could also significantly delay the next glacial period. This was later confirmed by other studies (Ganopolski et al., 2016; Talento and Ganopolski, 2021).

In the past, general circulation models (GCMs) and intermediate complexity models (EMICs) have been used to study the 1000–10,000 year carbon cycle response to anthropogenic CO_2 emissions (see: Archer et al., 2009a; Joos et al., 2013). Modelling studies become more scarce when going even further forward in time due to the rising computational cost, and as such, experiments are based on either EMICs (Ridgwell and Hargreaves, 2007; Charbit et al., 2008; Eby et al., 2009; Shaffer, 2010; Goodwin and Ridgwell, 2010; Meissner et al., 2012; Ganopolski et al., 2016; Brault et al., 2017; Jeltsch-Thömmes and Joos, 2020; Duque-Villegas et al., 2022), or models of lower complexity (Sundquist, 1991; Walker and Kasting, 1992; Lenton and Britton, 2006; Tyrrell et al., 2007a; Uchikawa and Zeebe, 2008; Cawley, 2011; Herrero et al., 2013; Köhler, 2020; Talento and Ganopolski, 2021; Couplet et al., 2024). The results of these studies largely agree in some aspects. For example, it has been established that the magnitude of cumulative emissions will predominantly control the long-term response, rather than the emission pathway (Eby et al., 2009; Matthews et al., 2009; Zickfeld et al., 2012; Herrington and Zickfeld, 2014). Contemporary predictions for deep future CO_2 concentrations exhibit considerable diversity, however. For illustration, Fig. 1 provides a graphical overview on the current estimates of atmospheric CO_2 concentration 10,000 years after present for different cumulative CO_2 emissions.

Quantifying the atmospheric lifetime of anthropogenic CO_2 is challenging because it is controlled by a number of biochemical and geological mechanisms operating on different timescales up to hundreds of thousands of years (Archer et al., 2009a). Modelling studies suggest that the terrestrial biosphere will initially uptake anthropogenic CO_2 (owing to enhanced vegetation productivity from CO_2 fertilization), although increased cellular respiration, soil carbon decomposition, land-use change, and wildfires could eventually turn the land into a carbon source in a warming world. Extensive fossil fuel emissions can therefore

---

[1]Here, we follow terminology introduced by Archer and Brovkin (2008), where "lifetime of anthropogenic CO_2" is understood to be the lifetime of an anomaly in atmospheric CO_2 concentration caused by anthropogenic CO_2 emissions.
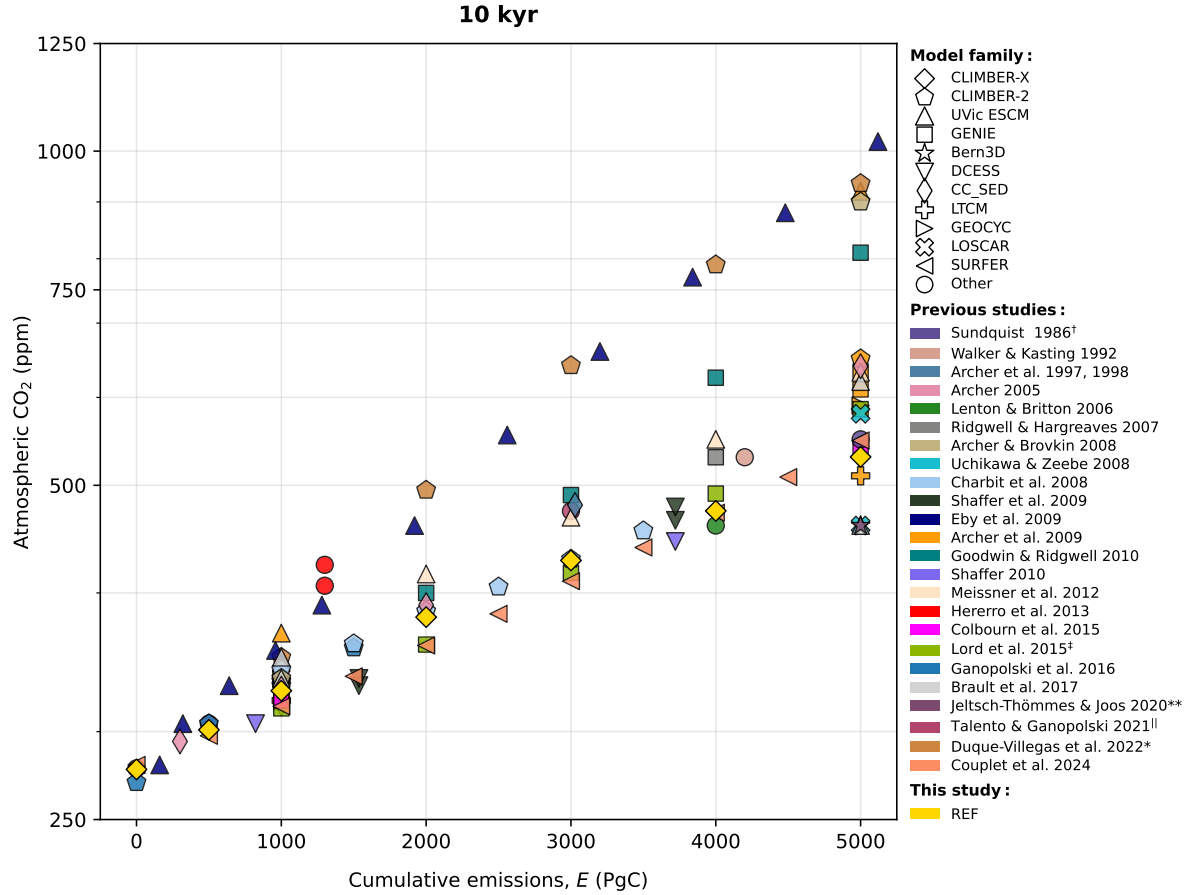
Figure 1. Estimates on the impact of different cumulative emissions on atmospheric CO_2 **concentration 10** kyr **after the start of the simulation.** The data from previous studies shown here was acquired through visual inspection of graphs, meaning that the figure is semi-qualitative and mostly serves an illustrative purpose (small errors may be present). Experiments shorter than 10,000 years, or those which considered emissions of 6,000 PgC or larger (i.e., unconventional fossil fuel resources), were omitted. Different experiments were chosen from these publications to highlight that the large diversity is primarily due to how long-term carbon cycle processes are resolved. The reference experiment in this study (yellow) has been plotted for comparison. Further information can be found in the respective publications.[†]Data for Sundquist (1991) taken from Tyrrell et al. (2007a). [‡]Data generated from the emulator based on cGENIE results. [**]Data calculated from fraction of emissions remaining. [‖]Best solution from the model ensemble. [*]Data calculated from formula provided in the appendix.

overpower the capacity of conventional land carbon reservoirs to absorb anthropogenic CO_2, and only the ocean remains the CO_2 sink on long timescales through processes such as air–sea CO_2 exchange, ocean invasion, seafloor $CaCO_3$ reactions and carbonate accumulation. The substantial influence that marine biogeochemistry has on the long-term carbon cycle has also been recognized by many studies, particularly regarding the reaction between dissolved anthropogenic CO_2 and calcium car-
60   bonate in deep ocean sediments (Archer et al., 1997; Middelburg et al., 2020). On even longer timescales, carbon exchange with geological reservoirs becomes important through processes such as sediment burial, chemical weathering of rocks on land, and volcanic degassing. As a consequence of all of these processes, carbon cycle models predict a highly nonlinear removal of anthropogenic CO_2 over time. The decline in anthropogenic CO_2 is usually presented as a superposition of exponential decays (Maier-Reimer and Hasselmann, 1987; Archer et al., 1997; Archer and Brovkin, 2008; Colbourn et al., 2015; Lord et al.,
65   2015b), with each function representing a different process in the carbon cycle that takes up carbon. This generally produces a "long tail" of anthropogenic CO_2 concentration which has been shown to persist for hundreds of thousands of years.

Due to the complexity and variety of poorly understood processes, the long-term future climate evolution remains highly uncertain even without considering the unpredictability of future anthropogenic emissions (which can be reconciled to some extent using an ensemble of emission scenarios). Given this complexity, it becomes essential to make assumptions based on the
70   timescales involved, the specific research question being addressed, and the resolution of the model employed. Previous studies have often made significant simplifications to (e.g., Lenton and Britton, 2006), or completely neglected (e.g., Archer et al., 1997; Lord et al., 2015b; Köhler, 2020) certain aspects related to land carbon. Weathering processes have also been frequently simplified (e.g., Charbit et al., 2008; Uchikawa and Zeebe, 2008), or their feedbacks not considered (e.g., Montenegro et al., 2007; Ridgwell and Hargreaves, 2007; Eby et al., 2009). As computational expense is the biggest factor inhibiting high-
75   resolution modelling on longer timescales, these studies also did not consider the interaction between CO_2 and ice sheets, methane deposits, and the effect of future glacial cycles (Archer, 2005).

Here, we provide a set of idealized long-term transient climate change scenarios for the next 100,000 years using the fast Earth system model CLIMBER-X with a comprehensive carbon cycle model. These experiments seek to quantify the degree of uncertainty of the "anthropogenic factor" by employing a wide range of idealized emission scenarios to evaluate the spread
80   in possible climate response. Considering the ongoing and substantial disagreement of future CO_2 evolution among different models, we provide an analysis of the sensitivity of the model response to climate sensitivity and different carbon cycle processes. This is a first step towards a fully-coupled simulation of the next 100 kyr with CLIMBER-X that includes interactive ice sheets. The paper is structured as follows: we first describe our experimental set-up, model, and considerations (Section 2). The results are then contextualized in relation to other studies by analyzing the model response, atmospheric lifetime, and
85   subsequent removal timescales of different carbon cycle processes (Section 3). This is followed by a corresponding sensitivity study (Section 4). We conclude with a brief discussion, summary of our findings and and an outlook on further investigations (Section 5).

2 Methods

2.1 Model description

We use CLIMBER-X v1.1 (Willeit et al., 2022, 2023), a fast Earth system model designed to simulate the climate evolution on time scales ranging from decades to >100,000 years. CLIMBER-X includes the statistical-dynamical semi-empirical atmosphere model SESAM (Willeit et al., 2022), the 3D frictional-geostrophic ocean model GOLDSTEIN (Edwards et al., 1998; Edwards and Marsh, 2005), the dynamic-thermodynamic sea ice model SISIM (Willeit et al., 2022), the land surface and dynamic vegetation model PALADYN (Willeit and Ganopolski, 2016) and the ocean biogeochemistry and marine sediments model HAMOCC (Heinze and Maier-Reimer, 1999; Ilyina et al., 2013; Mauritsen et al., 2019). CLIMBER-X operates at a horizontal resolution of $5° \times 5°$. It is computationally efficient and can simulate up to 10,000 years per day, allowing it to perform a large ensemble of long-term simulations. This is also possible because short term processes (e.g., weather, diurnal cycle) are not resolved. CLIMBER-X can generally well represent historical changes in climate (Willeit et al., 2022) and the carbon cycle (Willeit et al., 2023), and is suited to provide credible simulations for very long timescales into the deep future. Some studies using CLIMBER-X to transiently simulate the next several thousand years with a focus on the stability of the Greenland ice sheet have already been performed (e.g., Höning et al., 2023; Höning et al., 2024).

2.2 Open carbon cycle

The CLIMBER-X carbon cycle model has already been described in detail (Willeit et al., 2023), and has been shown to effectively represent the cycling of carbon though the atmosphere, vegetation, soils, permafrost, seawater, and marine sediments. For our experiments, we run the simulations using the so-called "open carbon cycle set-up" (Willeit et al., 2023), with interactive marine sediments, weathering on land, and the resulting geological sources and sinks of carbon. Carbon is not conserved in this setup; it is removed from the system through sediment burial and introduced to the system via weathering, volcanic outgassing, and through anthropogenic emissions. In the open carbon cycle setup, a simplification is made to enforce that the budgets for silicate and phosphorus within the ocean–sediment system are balanced. This was done by disabling riverine fluxes of phosphorus and silicate, and assuming that organic carbon (which includes P) and opal (which includes Si) which are buried in the sediments (and, therefore, removed from the system) are instead returned to the surface ocean in remineralized form. The conservation of such inventories in the ocean–sediment system removes challenges related to nutrient conservation that would otherwise complicate the analysis and interpretation of model results. The globally uniform atmospheric CO_2 concentration in CLIMBER-X is computed interactively using source and sink terms in the following prognostic equation for the total carbon content stored as atmospheric CO_2 (C_{atm}, in PgC):

$$\frac{dC_{atm}}{dt} = F_{lnd} + F_{ocn} + F_{anth} + F_{volc} - F_{weath} \tag{1}$$

where F_{lnd} is the global net land-to-atmosphere carbon flux (PgC yr^{-1}), F_{ocn} is the net sea-air carbon flux (PgC yr^{-1}),
F_{anth} are anthropogenic carbon emissions (PgC yr^{-1}), F_{volc} is the volcanic outgassing flux (PgC yr^{-1}), and F_{weath} is the CO_2
consumption by carbonate and silicate weathering (PgC yr^{-1}) (Willeit et al., 2023). PALADYN includes a rock weathering
scheme influenced by runoff and temperature (Hartmann, 2009a; Börker et al., 2020), accounting for 14 different lithologies
as described in Hartmann and Moosdorf (2012). The weathering module computes dissolved inorganic carbon (DIC) and
alkalinity fluxes to the ocean based on the release of bicarbonate ions (HCO_3^-) into rivers. Spatially explicit carbonate and
silicate weathering fluxes take the form:

$$F_{weath}^{carb} = F_{weath,0}^{carb} \sum_{\ell=1}^{13} \begin{cases} \beta(\ell) \times \left(3.1692 \times 10^{-3}\right) R_{off} & \text{for } \ell = \text{carbonate sedimentary rock,} \\ \beta(\ell) \times 10^{-6} 10^{9\left(1+e^{-0.63(\log_{10} R_{off}+0.76)}\right)^{-1}-2} & \text{for } \ell = \text{loess,} \\ \beta(\ell)\alpha(\ell) \times b(\ell) \times e^{\frac{1000\, E_{a,carb}}{R(T \cdot T_0)}(T-T_0)} R_{off} & \text{for } \ell = \text{other lithologies (Table E1),} \end{cases} \tag{2}$$

$$F_{weath}^{sil} = F_{weath,0}^{sil} \sum_{\ell=1}^{13} \beta(\ell)(1-\alpha(\ell)) \times b(\ell) \times e^{\frac{1000\, E_{a,sil}(\ell)}{R(T \cdot T_0)}(T-T_0)} R_{off}, \tag{3}$$

Weathering fluxes are largely described by the Arrhenius equation, with the exception of carbonate weathering for carbonate
sedimentary rocks and loess, which are instead described by the runoff-dependent weathering equations from Amiotte Suchet
and Probst (1995) and Börker et al. (2020), respectively. In Equations 2 and 3, ℓ represents the different lithologies, T is the
annual mean near-surface air temperature (K), T_0 is 284.2 K, R_{off} is the annual runoff (kg m^{-2} yr^{-1}), $b(\ell)$ is the molality/weath-
ering rate (molC kg^{-1} water), $E_{a,carb}$ is the activation energy of carbonates (14 kJ mol^{-1}), $E_{a,sil}(\ell)$ is the activation energy of
silicates (kJ mol^{-1}), R is the molar gas constant (8.3145 J mol^{-1} K^{-1}), $\alpha(\ell)$ is the fraction to weather as carbonate rocks, and
$\beta(\ell)$ is the fraction of a given lithology in a grid cell (Fig. E1). The values for α, b, and E_a are all based on the calibrated runoff
and temperature dependent models from Hartmann (2009a) and Hartmann et al. (2014), and are displayed in Table E1.

Although the Earth experiences a number of external forces, this study generally excludes factors like impact events, changes
in tectonic configuration and solar luminosity, as they are either unpredictable or operate on such long timescales that they are
not relevant for our investigation. Similarly, we do not resolve the "deep" carbon cycle (i.e., carbon subduction and recycling
in the Earth's mantle) as their effects only become important on timescales longer than our experiment duration (i.e., $10^6 - 10^7$
years), and involves processes that cannot be resolved with Earth system models. As such, we assume that the pre-industrial
carbon cycle was in equilibrium, which implies that the constant volcanic outgassing is prescribed and set to half the global
silicate weathering flux at the pre-industrial time (0.0738 PgC yr^{-1} or 6.15 TmolC yr^{-1}). This condition ensures that the at-
mospheric CO_2 is in equilibrium under pre-industrial conditions (Munhoven and François, 1994; Willeit et al., 2023), which
has been a common assumption in previous investigations which looked at the long-term forced response of the climate (e.g.,
Colbourn et al., 2015; Lord et al., 2015b).

Table 1. Overview of the experimental configuration for the simulations performed in this study. For each experimental configuration, all emission forcings (0 PgC-5000 PgC) were applied to produce an ensemble. Emissions pathways are shown in Fig. E2.

Experiment Name	Emission Pathway	Land Carbon	Terrestrial Weathering	Climate Sensitivity	Methane
Reference experiment					
REF	Control	On	Variable	3.1°C	Constant
Emission pathway experiments					
PULSE	Pulse	On	Variable	3.1°C	Constant
PATH1	Fast	On	Variable	3.1°C	Constant
PATH2	Slow	On	Variable	3.1°C	Constant
Sensitivity experiments					
noLAND	Control	Off	Variable	3.1°C	Constant
noWEATH	Control	On	Constant	3.1°C	Constant
ECS2	Control	On	Variable	2°C	Constant
ECS4	Control	On	Variable	4°C	Constant
intCH4	Control	On	Variable	3.1°C	Interactive

2.3 Experimental set-up

Model simulations are started from a pre-industrial equilibrium state which has been obtained from a 100,000 year equilibrium spin-up of the carbon cycle model as described in Willeit et al. (2023). The pre-industrial CO_2 concentration is taken to be 280 ppm, whereas the pre-industrial orbital parameters of eccentricity e is 0.0167, obliquity ε is 23.46°, and the perihelion ω is 100.33°. This corresponds to a maximum summer insolation at 65°N of 480.4 Wm^{-2}. In the reference experiment, we set a constant methane concentration of 600 ppb, which is representative for Holocene conditions (Sapart et al., 2012; Mitchell et al., 2013; Beck et al., 2018). Although CLIMBER-X is capable of simulating ice sheets (e.g., Höning et al., 2023; Talento et al., 2024; Willeit et al., 2024), we conduct our simulations with prescribed present-day Greenland and Antarctica to ensure comparability with earlier studies. Interactive ice sheets will be enabled in a follow-up study. To simplify interpretation and ensure consistency with previous studies, orbital forcing was fixed at present-day values, with the combined effects of anthropogenic and orbital forcing to be explored in a future study. All simulations run for 100,000 years with constant orbital parameters and without any climate acceleration technique.

To investigate the lifetime of anthropogenic CO_2 and the effect it has on the long-term evolution of the climate, we introduce idealized CO_2 emission scenarios representing cumulative emissions from 0 PgC to 5000 PgC (Fig. E2) to cover a variety of different anthropogenic scenarios. The upper limit of ∼5000 PgC has been used in many previous studies (e.g., Archer, 2005; Montenegro et al., 2007; Uchikawa and Zeebe, 2008; Archer et al., 2009a) as it just surpasses the current estimated maximum of conventional fossil fuel reserves (Lal, 2008; McGlade and Ekins, 2015). To simulate a variety of emissions pathways and explore the sensitivity of the results to the duration of the CO_2 emission pulse, we designed three different Gaussian functions

with different shapes (with an increasing mean and standard deviation with higher cumulative CO_2, Fig. E2), and one pulse-like perturbation where all emissions are released within the first year of the simulation. It should be noted here that the 100 kyr simulation duration includes the ramp up and ramp down of emissions. Following the emission function, emissions are set to 0 PgC yr^{-1} for the rest of the simulation.

170   A number of additional experiments were performed to isolate the effect of different carbon cycle processes on the long-term fate of anthropogenic CO_2. Specifically, we explored the role of the land carbon cycle response (noLAND), the impact of enabling interactive methane concentrations in the atmosphere (intCH4), and the impact of the emissions pathway (PULSE, PATH1, PATH2) on the lifetime of anthropogenic CO_2. To isolate the effect of the weathering feedback on the CO_2 lifetime, a dedicated set of experiments (noWEATH) was conducted in which weathering fluxes were enforced to remain constant at their

175   pre-industrial rate throughout the simulation (0.2376 PgC yr^{-1} or 19.8 TmolC yr^{-1} for carbonate weathering; 0.1476 PgC yr^{-1} or 12.3 TmolC yr^{-1} for silicate weathering). The sensitivity of the results to different equilibrium climate sensitivities (ECS) between 2-4 °C was additionally investigated (ECS2, ECS4) by rescaling the equivalent CO_2 in the long-wave radiation scheme (further described in Appendix A). A summary of all experimental configurations is presented in Table 1.

3   Results

180   ### 3.1   Long-term carbon cycle evolution

An overview of the 100 kyr response in atmospheric CO_2 concentration and global mean temperature across all emission scenarios in the reference (REF) experiment can be seen in Fig. 2. The initialization of our experimental set-up is demonstrably robust, evidenced by the less than 2 ppm drift (from the pre-industrial 280 ppm) of atmospheric CO_2 concentration in the zero emissions scenario over the span of 100 kyr (Fig. 2a). All simulations with anthropogenic emissions show a rapid increase in

185   atmospheric CO_2 concentration during the ramp up of emissions, with peak concentration occurring within the first 200 years. In the REF experiment, peak CO_2 concentrations fall between ∼360-1820 ppm across the different emission scenarios (Fig. 2a). These values are within the range of magnitude reported by previous studies (e.g., Montenegro et al., 2007; Colbourn et al., 2015). We find that the increase in global mean surface temperature lags that of CO_2 concentration (Fig. 2b), and that the size of the temporal lag tends to increase as cumulative emission grows (Ricke and Caldeira, 2014; Zickfeld and Herrington, 2015).

190   Peak temperature anomalies range between ∼0.6-6.4 °C across the different emission scenarios in the REF ensemble. After 300 years from the start of the experiments, both atmospheric CO_2 concentration and global temperatures decrease as carbon is taken up by the land and ocean pools. The only exception to this is the 5000 PgC scenario, where temperatures temporarily stabilize instead of decreasing (Fig. 2a-c). This is largely due to the extended decline in the Atlantic Meridional Overturning Circulation (AMOC; Fig. 7e), which results in a cooling in the Northern Hemisphere that prevents global mean temperature

195   from further rising. Temperatures slowly decrease towards to pre-industrial levels and, after 10 kyr, global warming is reduced by more than half (Fig. 2b). After 100 kyr, atmospheric CO_2 concentration still remains ∼10-100 ppm above pre-industrial levels across the different emission scenarios, and temperatures are still between ∼0.1-1.4 °C larger than the pre-industrial at the end of the simulation.
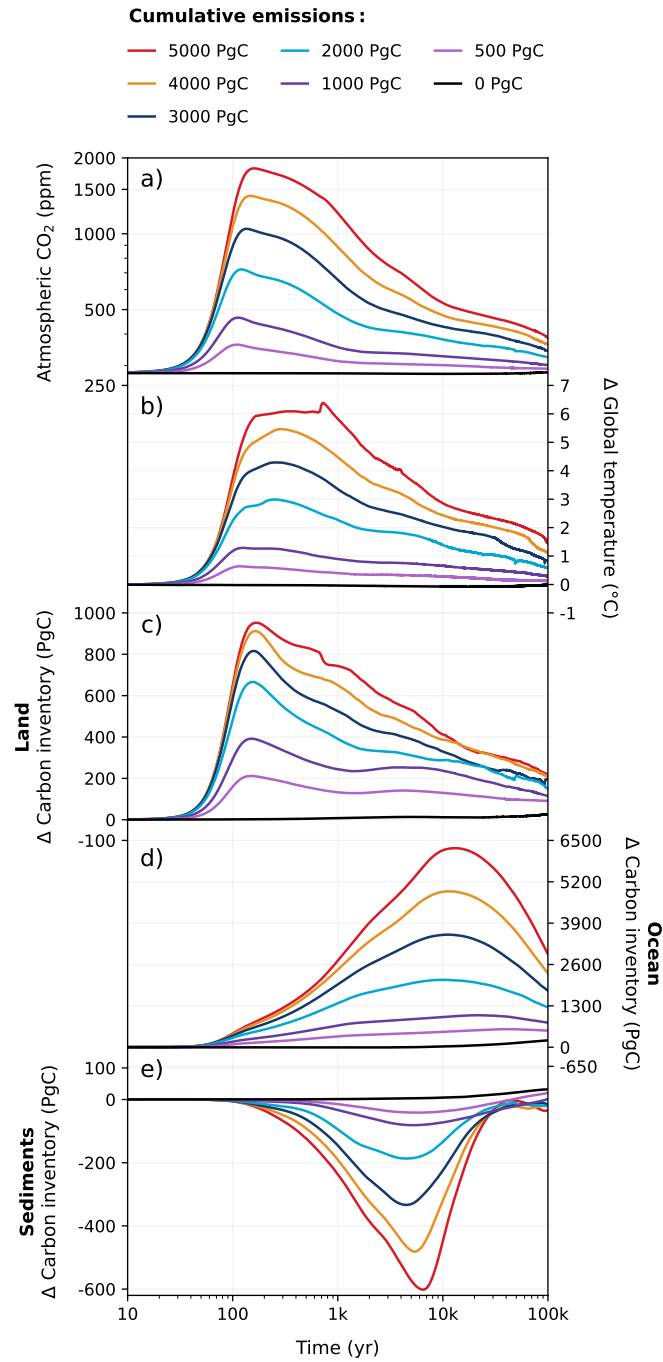
Figure 2. Response in (a) atmospheric CO_2 **concentration, (b) global surface air temperature, (c) land carbon inventory, (d) ocean carbon inventory, and (e) sediment carbon inventory to the full ensemble of emission scenarios (0-5000** PgC**) in the REF experiment for 100** kyr**.**
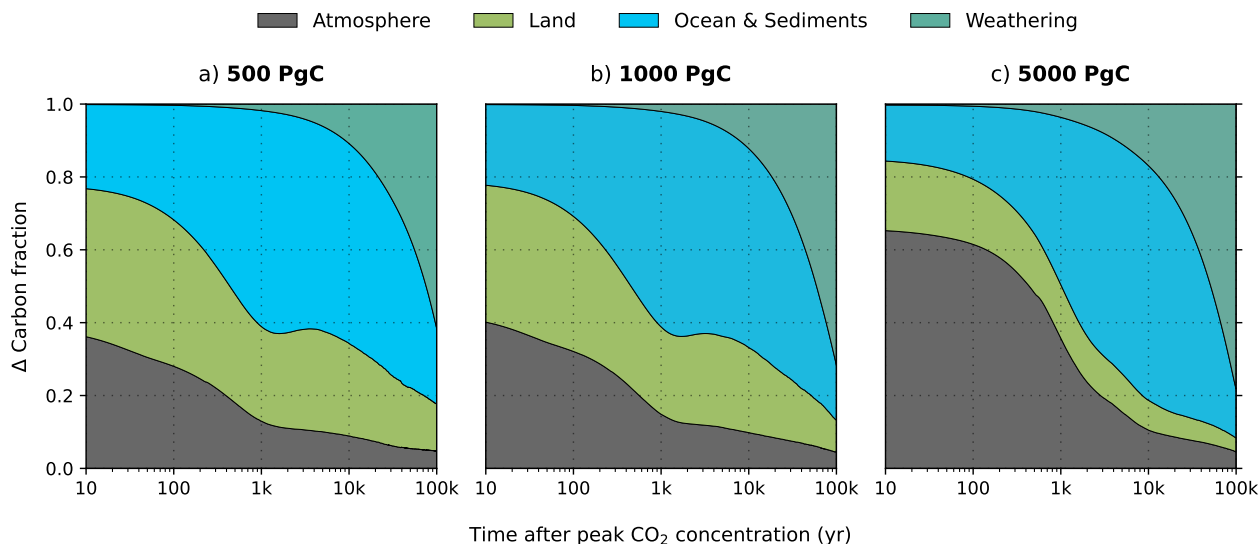
Figure 3. The relative partition of anthropogenic carbon in the REF experiment after peak atmospheric CO_2 **concentration.** The partition of the atmosphere (grey), land (green), ocean & sediments (blue) and silicate weathering (teal) is shown for the (a) 500, (b) 1000, and (c) 5000 PgC scenarios. These calculation for these percentages is outlined in Appendix B using cumulative fluxes from the atmosphere. The carbon fraction attributed to the ocean & sediments is labeled this way, as the air–sea CO_2 flux may indirectly include carbon from sediments through dissolution. However, we do not account for sediment carbon fluxes directly since there is no direct air–sediment flux (see Appendix B for further details on this formulation). It should be noted that the ramp up of emissions is excluded here.

The fate of the anthropogenic CO_2 emissions (and how this carbon is distributed among the different Earth system compo-
200   nents) after the peak atmospheric CO_2 concentration is shown in Fig. 3. The land and ocean both rapidly absorb CO_2 during the ramp up of emissions through enhanced vegetation productivity, air–sea CO_2 exchange and its subsequent dissolution (Fig. 4). At peak CO_2 concentrations, the land and ocean are responsible for between 34–61% of carbon removal (19–39% by land, 15–22% by the ocean, Fig. 3), with the carbon removal fractions decreasing with increasing cumulative emission. During the first 1 kyr after peak CO_2 concentrations, oceanic CO_2 uptake gradually slows as surface waters approach equilibrium with
205   the atmosphere (Fig. 4b). Although ocean carbon fraction largely increases over the first 1 kyr after peak CO_2 concentrations (accounting for 46–59% 1 kyr after emissions cease, Fig. 3), the carbon fraction taken up by the ocean during the latter half of the millennium appears disproportionately larger than what is taken up during the first 500 years, as land carbon already begins decreasing by this time (Fig. 2c, Fig. 4a). Beyond the first millennium, geological processes (e.g., marine sediments and weathering) largely control the evolution of atmospheric CO_2 concentration (Archer and Brovkin, 2008). Silicate weathering is
210   responsible for 11–17% of carbon removal 10 kyr after peak CO_2 concentration. However, by 100 kyr, it is responsible for the majority of carbon removal (62–78%), and becomes the dominant removal process on the timescale of hundreds of thousands of years.
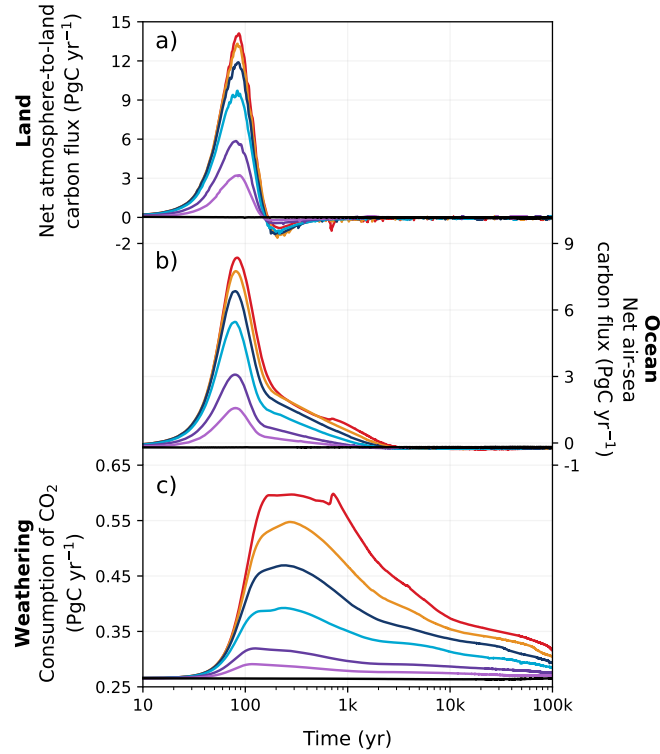
Figure 4. Changes in (a) net atmosphere-to-land carbon flux, (b) net air–sea carbon flux, and (c) weathering consumption of CO_2 **in different emission scenarios over 100** kyr**.** Colours correspond to the cumulative emission scenarios shown in Fig. 2.

3.1.1 Land carbon response

Two opposing mechanisms involving vegetation and soil carbon predominantly govern the land carbon response to climate
215 change. The land carbon pool (as the sum of vegetation and soil carbon) is initially a carbon sink due to increases in vegetation
carbon (Brovkin et al., 2013), as CO_2-driven fertilization enhances net primary productivity. These increases, however, can
be partially or totally offset by warming-enhanced soil respiration, which strongly depends on model parameters, whether
permafrost, peatlands, and wetlands are included, and how they are modelled in the carbon cycle model (Zickfeld et al., 2013;
Eby et al., 2013). In our simulations, the peak increase in vegetation carbon significantly exceeds and more than compensates
220 for the maximum loss in soil carbon (Fig. 5). Peak land carbon uptake in our simulations falls comfortably between values
given by previous studies (Mikolajewicz et al., 2006; Vakilifard et al., 2022).

In the latter half of the first millennium, vegetation carbon decreases as atmospheric CO_2 concentrations fall (Fig. 5a). Soil
carbon exhibits non-monotonous behaviour with increasing emissions: low emission scenarios (<1000 PgC) have gained up
to 100 PgC, and high emission scenarios (>4000 PgC) have lost up to 150 PgC by 1 kyr (Fig. 5b). This is because, in the
225 low emission scenarios, the accumulation of carbon in soil exceeds carbon loss due to enhanced soil respiration (Fig. 6h),
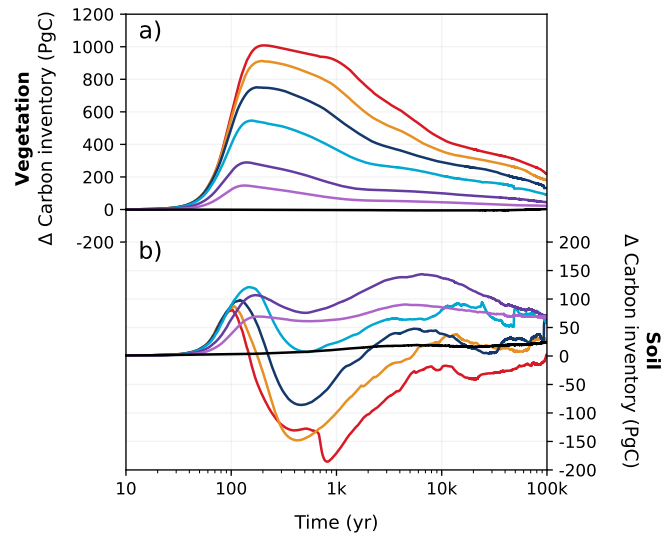
Figure 5. Changes in (a) vegetation and (b) soil carbon inventories relative to the pre-industrial period in different emission scenarios over 100 kyr**.** Colours correspond to the cumulative emission scenarios shown in Fig. 2.

preventing the overall decline in soil carbon inventory (Fig. 5b). This is not the case in high emission scenarios, as permafrost area decreases so significantly that soil respiration counteracts any potential increase when temperatures are sufficiently high (Fig. 6i). The increase in vegetation carbon is generally globally distributed with increasing emissions (Fig. 6e,f) largely because of increases in net primary productivity (Fig. 6b,c), although there are a few regions which are an exception due to
230   decreased precipitation (Fig. 11h,i). Although soil carbon inventory decreases in high emission scenarios by 1 kyr, it recovers over the next 100 kyr as temperatures gradually decrease. In our simulations, the terrestrial storage of anthropogenic carbon is positive during the entire 100 kyr due to an increase in vegetation carbon and recovery of soil carbon. At the end of the experiments, the land still stores approximately 7% (range 4–13%) of the emitted anthropogenic carbon (Fig. 3).

3.1.2   Ocean and sediment carbon response

235   The ocean absorbs and stores atmospheric CO_2 due to a sequence of chemical, biological, physical and geological processes. Under anthropogenic emissions, the ocean initially takes up carbon at an accelerated rate from greater air–sea CO_2 exchange (Fig. 4b). At peak CO_2 concentration, the ocean has a net cumulative uptake between $\sim$100–780 PgC depending on the emission scenario (Fig. 2d). Oceanic CO_2 uptake yields the production of bicarbonate and hydrogen ions from CO_2 dissolution. As a consequence, surface ocean pH decreases at a similar rate that carbon is taken up in the ocean, with larger pH decreases
240   associated with higher cumulative emissions (Fig. 7b). The magnitude of surface ocean pH decrease in our experiments match well with other studies: for example, the peak pH anomaly of approximately -0.7 in the 5000 PgC experiment falls within the range of -0.6 to -0.8 given by other models (Caldeira and Wickett, 2005; Montenegro et al., 2007; Uchikawa and Zeebe, 2008; Eby et al., 2009; Zickfeld et al., 2012; Colbourn et al., 2015). As phytoplankton growth rate strongly depends on temperature in
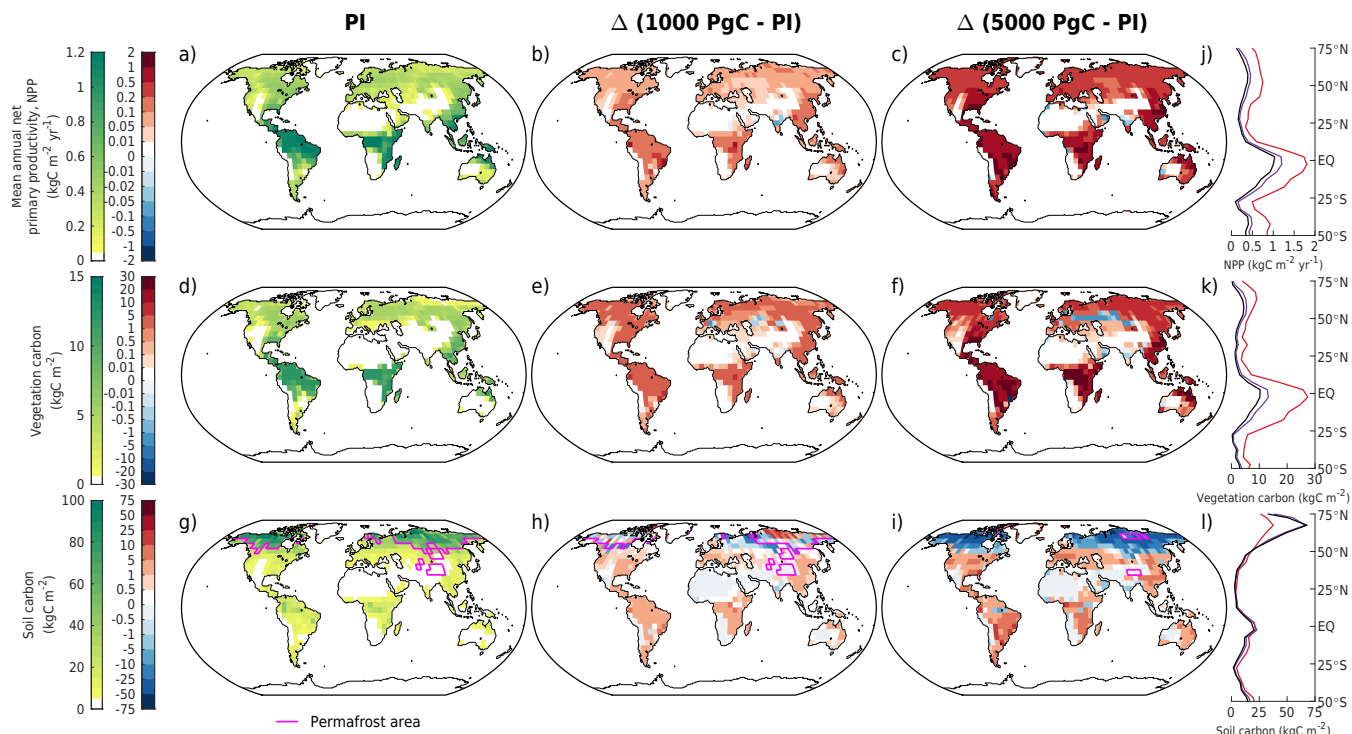
Figure 6. Mean annual (a-c) net primary productivity, (d-f) vegetation carbon, and (g-i) soil carbon in different emission scenarios at 1 kyr. The columns show (a,d,g) absolute values in the zero emissions scenario (equivalent to the pre-industrial), (b,e,h) 1000 PgC scenario relative to the pre-industrial, and (c,f,i) 5000 PgC scenario relative to the pre-industrial. Absolute values for the zonal mean are additionally shown for (j) NPP, (k) vegetation and (l) soil carbon for the zero emissions (black), 1000 PgC (purple), and 5000 PgC (red) scenarios. Magenta lines (g-i) display the permafrost area.

HAMOCC (Ilyina et al., 2013; Willeit et al., 2023), net primary productivity (NPP) generally increases with higher sea surface temperature (SST) under larger cumulative emissions (Fig. 8a). Warming also accelerates the remineralization of organic matter in the ocean, which increases nutrient availability in the surface ocean for primary production. Moreover, reduced sea-ice cover in high latitudes increases light availability and, therefore, enhances local productivity. In our highest emission scenario, the combined effects amount to an approximate ∼20% increase in peak NPP under the 5000 PgC scenario compared to the pre-industrial value (53.3 PgC yr^{-1}, Fig. 8a).

As the amount of dissolved CO_2 in the surface ocean rises, its ability to absorb excess CO_2 decreases. This decrease in buffering capacity is illustrated by the Revelle factor (ξ, the sensitivity of pCO_2 to changes in DIC; Revelle and Suess, 1957), which increases with higher emissions (Fig. 7a). The pre-industrial Revelle factor of ∼9.4 matches reasonably well with that calculated by Jiang et al. (2019), and the peak Revelle factor in the 500 PgC scenario (∼10.2) is close to that calculated using present-day GLODAPv2 observations (Terhaar et al., 2022). Between 100 yr and 1 kyr, ξ slowly decreases, owing to the gradual decrease of surface DIC (except for the 5000 PgC scenario, Fig. 7c) and the increase of surface alkalinity (Fig.
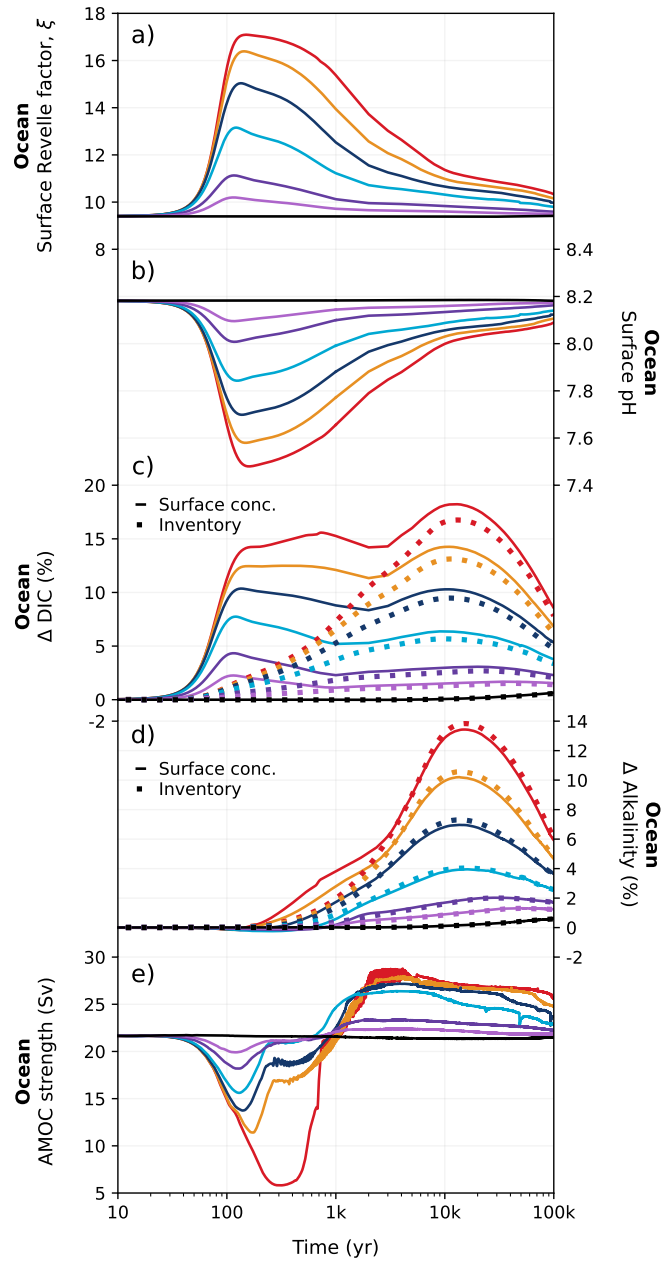
Figure 7. Changes in (a) ocean buffering capacity (Revelle factor), (b) global mean surface pH, (c) relative changes in surface DIC concentration and global ocean DIC inventory, (d) relative changes in surface alkalinity concentration and global alkalinity inventory, and (e) strength of the Atlantic Meridional Overturning Circulation (AMOC) in different emission scenarios over 100 kyr**.** Colours correspond to the cumulative emission scenarios shown in Fig. 2. The surface ocean Revelle factor shown in (a) has been calculated via Eq. C1 in Appendix C.
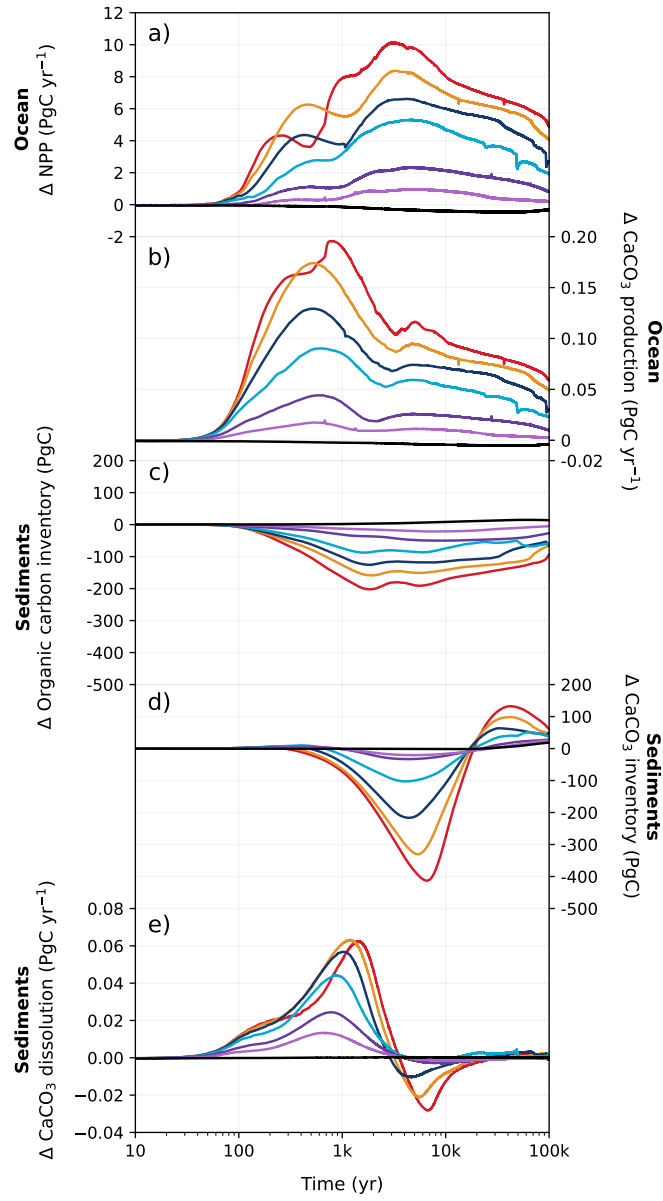
Figure 8. Changes in (a) marine net primary production, (b) $CaCO_3$ **production, (c) sediment particulate organic carbon inventory, (d) sediment** $CaCO_3$ **inventory, and (e) sediment** $CaCO_3$ **dissolution rate in different emission scenarios over 100** kyr**.** Colours correspond to the cumulative emission scenarios shown in Fig. 2.

7d). The decrease of surface DIC results from the combined effect of the downward transport of anthropogenic carbon in the surface ocean and the enhanced biological production (Fig. 8a), which is partly counteracted by the increase of the global DIC inventory (Fig. 7c). Both DIC and alkalinity inventories increase during this period due to high carbonate weathering fluxes (input as HCO_3^- into the ocean, see Fig. 9a) and enhanced refluxes from sediment. Although NPP increases with warming, the loss of organic carbon to the sediment (not shown) and the organic carbon content in the sediment (Fig. 8c) are reduced due to higher remineralization rates in both the water column and sediment. Deep convection, which transports surface waters with decreased pH and carbonate ion concentrations into the interior ocean, together with increased organic matter remineralization, causes carbonate ion concentrations in the interior ocean to fall with increasing emissions (Fig. E5). In response, the lysocline and carbonate compensation depth (CCD) shoal and sediment $CaCO_3$ dissolves (contributing more to the total loss of sediment carbon inventory than sediment organic carbon, Fig. 2e), driving the increase of alkalinity inventory. In the 5000 PgC scenario, surface DIC increases between years 1100 to 1700, which is likely due to the extended period of AMOC decline (Fig. 7e) that inhibits deep convection and the downward carbon transport.

Surface DIC shows diverse variations between 1 and 10 kyr depending on the emission scenario, whereas surface alkalinity generally increases and is responsible for the recovery of the buffering capacity (shown by the continuous decline of ξ). The variation of surface alkalinity generally follows that of the global inventory, with the latter controlled by the weathering input and net loss to the sediment. The sediment $CaCO_3$ continues to dissolve with a higher rate than the first millennium (Fig. 8e). Beyond 10 kyr, both surface DIC and alkalinity decline, following the respective global inventory, as a response of decreased carbonate weathering (Fig. 9a) and increased loss to the sediment (Fig. 8c,d). Due to silicate weathering (Section 3.1.3) which reduces atmospheric CO_2, the ocean becomes a carbon source, contributing to the decrease of surface DIC and the recovery of buffering capacity. The impact of carbonate compensation and seafloor $CaCO_3$ neutralization on restoring the buffering capacity on millennium timescales shown in these simulations are in line with previous studies (Archer et al., 1997, 1998; Tyrrell et al., 2007a; Tyrrell, 2007b). The recovery of sediment $CaCO_3$ inventory occurs roughly around the same time as predicted by Lenton and Britton (2006). However, the timing of peak $CaCO_3$ dissolution in CLIMBER-X is earlier than in a CLIMBER-2 study by Montenegro et al. (2007), which may be due increased biological production of $CaCO_3$ (as it is proportional organic detritus production, and thus, net primary production, Fig. 8a) leading to more $CaCO_3$ export to the interior ocean.

3.1.3 Weathering response

While the pre-industrial weathering fluxes in our simulations (19.8 Tmol C yr^{-1} for carbonate, 12.3 Tmol C yr^{-1} for silicate; Fig. 9) fall within, but toward the higher end of, observational estimates (Meybeck, 1987; Gaillardet et al., 1999; Munhoven, 2002; Amiotte Suchet et al., 2003), they are significantly higher than previous studies investigating the long-term future CO_2 evolution (Uchikawa and Zeebe, 2008; Colbourn et al., 2015; Lord et al., 2015b). This is at least partly due to the spatially explicit weathering scheme employed in our model, as switching from a 0D to a 2D scheme has been shown to increase global weathering rates (Colbourn, 2011; Colbourn et al., 2013). Chemical weathering on land increases in high emission scenarios due to warmer and wetter conditions, drawing down more carbon from the atmosphere (Fig. 9). Both carbonate and silicate
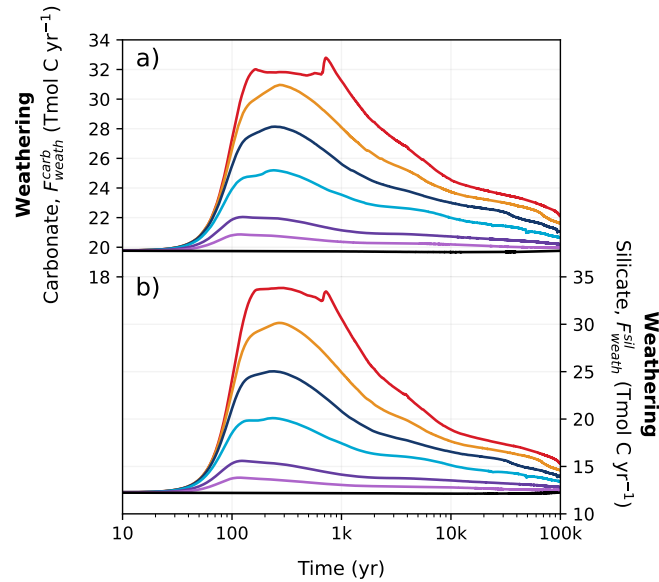
Figure 9. Changes in (a) carbonate and (b) silicate weathering fluxes in different emission scenarios over 100 kyr**.** Colours correspond to the cumulative emission scenarios shown in Fig.2.

290 weathering rapidly increase over the first 200 years, as a response to elevated temperatures and increased runoff (Lenton and Britton, 2006). Carbonate weathering flux increases to 20.8-32.0 Tmol C yr^{-1} in the different scenarios around the same time as peak atmospheric CO_2 concentration (Fig. 9a). Peak silicate weathering occurs at the same time, but has even larger differences from the pre-industrial, nearly tripling under the high emission scenario (Fig. 9b). After peak weathering fluxes are reached in the REF experiments, they begin to decrease within the first millennium as atmospheric CO_2 decreases.

295 The sensitivity of carbonate and silicate weathering to climate change in CLIMBER-X is compared to estimates from earlier investigations in Fig. 10a,b. Generally, the CLIMBER-X response falls in between that what is estimated by previous studies (Sundquist, 1991; Uchikawa and Zeebe, 2008; Colbourn et al., 2015; Lord et al., 2015b), with the response of carbonate weathering falling in the middle, and silicate weathering tending to the stronger side. In both cases, however, weathering response is higher than simulated by the equations used in Lord et al. (2015b). In addition to this, the more sophisticated

300 weathering scheme in CLIMBER-X produces a narrow hysteresis in the response to the change in global mean temperature (Fig. 10a,b), as weathering fluxes decrease slower than global mean temperature. This hysteresis is primarily due to a lag between the evolution of precipitation and temperature. The combination of rather large pre-industrial silicate weathering flux and large sensitivity of silicate weathering to climate in the model results in a weathering feedback that is stronger than in some previous studies (Lord et al., 2015b; Colbourn et al., 2015). This has implications for the lifetime of atmospheric CO_2 (Section

305 3.2).

Most previous studies on deep future CO_2 concentrations did not spatially resolve weathering, instead relying on global mean values. The few studies which did use spatially explicit weathering employed either the GKWM (Bluth and Kump, 1991)
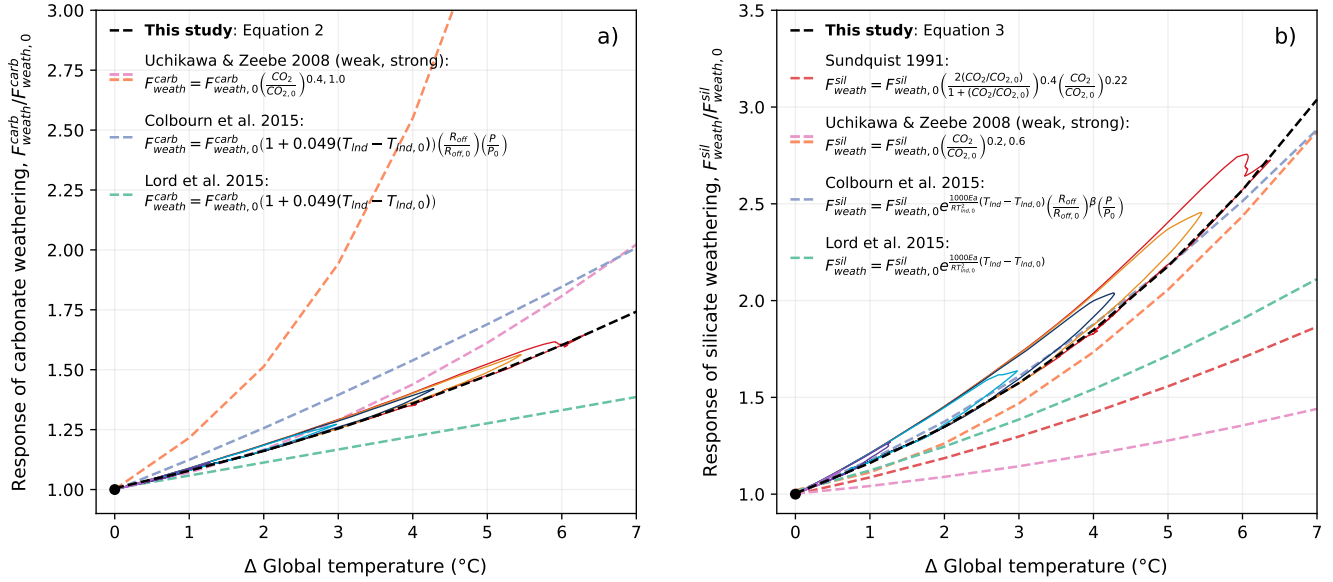
Figure 10. Relationship between (a) carbonate weathering, (b) silicate weathering, and temperature in previous studies and CLIMBER-X. Solid coloured lines corresponding to the cumulative emission scenarios seen in Fig. 2 represent the weathering response in the REF experiment. The black dashed line in (a) and (b) show an exponential fit of the trajectory of the weathering response. Calculated trajectories have additionally been plotted for the equations used by Sundquist (1991), Uchikawa and Zeebe (2008), Colbourn et al. (2015) (with runoff, R_{off}, and productivity, P, parametrized as a function of CO_2 as in Colbourn et al. (2013)), and Lord et al. (2015b) specifically using CLIMBER-X variables for atmospheric CO_2 (CO_2) and land surface temperature (T_{lnd}). The fit of these trajectories has been plotted above using *Numpy.Polyfit* in Python. It should be noted that, since this comparison is based on the simulated CLIMBER-X variables, it implicitly assumes an ECS of 3.1 °C.

or GEM-CO2 (Amiotte Suchet et al., 2003) lithological maps, which are quite coarse resolution compared to the GLiM (Hartmann, 2009a) lithological map used by CLIMBER-X. The pre-industrial carbonate and silicate weathering distributions are

310   shown in Fig. 11a,d. These distributions align quite closely with the calculated distribution of CO_2 consumption from Hartmann et al. (2009b). However, not all details can be reproduced given the 5°×5°resolution of CLIMBER-X and biases in precipitation (Fig. 11g, see Willeit et al. (2022)). Weathering rates rise with increasing temperature, particularly in regions where significant weathering is already taking place. Runoff, which indirectly depends on precipitation through soil infiltration and drainage (Willeit and Ganopolski, 2016), drives some of these changes (Fig. 11g,h,i, Fig. E6). As emissions grow, silicate weathering

315   sees a significant increase in the Tropical rain belt area due to higher precipitation. These include regions such as South East Asia, Central Africa, and Brazil (Fig. 11k). Large changes in carbonate weathering are more globally distributed than silicate weathering (Fig. 11e,f). However, like silicate weathering, large changes in carbonate weathering (e.g., increases and decreases in carbonate weathering in South East Asia and Central Asia compared to the pre-industrial) can also be explained by increases and decreases in precipitation (Fig. 11b,c). Such spatial patterns in silicate and carbonate weathering under idealized 1000
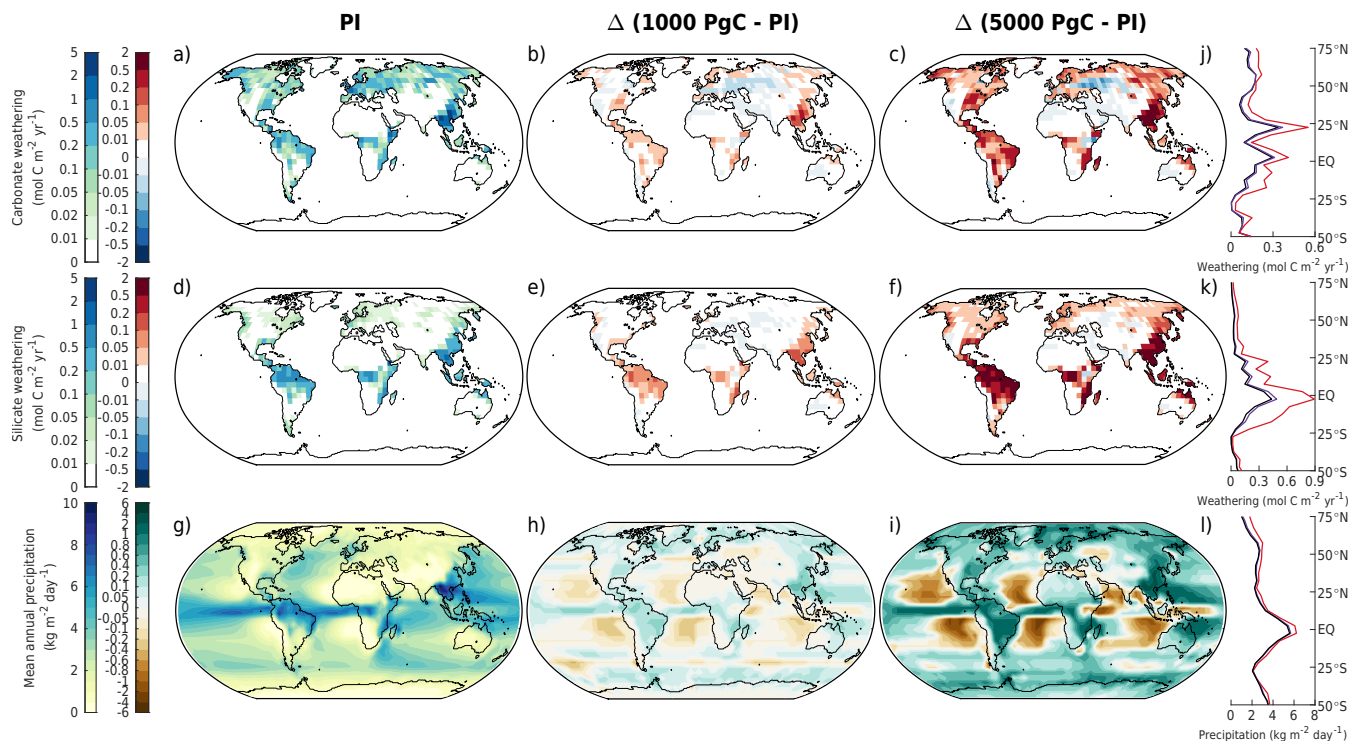
Figure 11. Mean annual (a-c) carbonate weathering, (d-f) silicate weathering and (g-i) precipitation in different emission scenarios at 1 kyr. The columns show (a,d,g) absolute values in the zero emissions scenario (equivalent to the pre-industrial), (b,e,h) 1000 PgC scenario relative to the pre-industrial, and (c,f,i) 5000 PgC scenario relative to the pre-industrial. Absolute values for the zonal mean are additionally shown for (j) carbonate weathering, (k) silicate weathering, and (l) precipitation for the zero emissions (black), 1000 PgC (purple), and 5000 PgC (red) scenarios.

320 and 5000 PgC scenarios have also been seen by Brault et al. (2017). In our simulations, highly active weathering regions are dominant contributors to the global weathering flux. About 10% of land area across the different emission scenarios is responsible for ∼13-14% of the total carbonate weathering and ∼33-37% of the total silicate weathering (Fig. 11b,c,e,f). Given that the simulated weathering rates for both carbonate and silicate rocks are quite heterogeneous spatially, simplifications used by previous studies to calculate weathering rates (e.g., weathering as a function of global mean land surface temperature) could 325 be insufficient to describe the feedback between climate and weathering.

3.2 Atmospheric lifetime of anthropogenic CO$_2$

The atmospheric lifetime of anthropogenic CO$_2$ across the different scenarios is estimated using an impulse response function (IRF). This is a first-order approximation on the long-term effects of a short term perturbation. It can be applied to changes in atmospheric CO$_2$ concentration (normalized by cumulative CO$_2$ emissions) such that it represents the fraction of emissions 330 remaining (Maier-Reimer and Hasselmann, 1987; Joos et al., 2013; Jeltsch-Thömmes and Joos, 2020). In this formulation, it

is functionally no different than airborne fraction, but we distinguish the two by assuming the IRF is only valid for time after peak CO_2 concentration ($CO_2(t_0) = CO_2^{max}$). This can be written as the following:

$$IRF_{CO_2}(t) = \frac{\Delta CO_2(t) \times 2.124}{E} \tag{4}$$

335

where E is cumulative emissions in PgC, $\Delta CO_2(t)$ is the change in atmospheric CO_2 concentration at time t compared to the pre-industrial concentration (280 ppm), and 2.214 PgC ppm^{-1} is the conversion factor between concentration and mass (Friedlingstein et al., 2023). The IRF for the REF ensemble is shown in Fig. 12. The ramp up of emissions is not included in this analysis. Unlike previous studies (e.g., Archer et al., 2009a; Joos et al., 2013), we do not deploy an instantaneous pulse, and
340   our fractions of emissions remaining do not start at 1 as carbon sequestration already began during the ramp up of emissions. While it is unlikely that the emissions pathway will be an important factor for the atmospheric lifetime on long timescales, the IRF for the PULSE, PATH1 and PATH2 experiments has additionally been plotted in Fig. 12b to explicitly show the impact of the emissions pathway. Although the emissions pathway has a notable impact on the IRF within the first millennium, this effect becomes largely negligible after ~3 kyr. This supports the long-term path independence found by Zickfeld et al. (2012)
345   and Herrington and Zickfeld (2014), meaning that, despite the potential complication from the ramp up and ramp down period of emissions in the REF experiment, our results are fully comparable with those in the Long-Term Model Intercomparison Project (LTMIP) in Archer et al. (2009a).

Modelling studies have suggested that the majority (up to 80%) of anthropogenic CO_2 is quickly taken up by fast carbon processes, leading to a mean lifetime of only a few centuries (Archer, 2005; Montenegro et al., 2007; Archer and Brovkin,
350   2008). In the REF experiment, the mean lifetime is 390 (range 0-955) years (Fig. 12c). This value depends on the cumulative emission loaded to the atmosphere (Fig. 12c), and to some extent, the pathway of the emission (Fig. 12b). This explains why the lifetime determined by the timing of $IRF_{CO_2}(t) = 1/e$ is close to zero in the 500 PgC scenario, as the majority of carbon is taken up from the atmosphere prior to reaching peak atmospheric CO_2 concentration in our simulations (Fig. 3c). On average, it takes between 197–1,820 years after peak CO_2 concentration to remove 75% of anthropogenic emissions, depending on the emission
355   scenario. Our results (Fig. 12c) generally agree with the most comprehensive assessment to date, which indicates that between 20-35% of CO_2 remains in the atmosphere after 200–2,000 years (Archer et al., 2009a). After 10 kyr, it has been previously reported that CO_2 emissions in the atmosphere would remain somewhere between ~5–20% for the 1000 PgC scenario and ~10–35% for 5000 PgC scenario (Archer et al., 2009a). In all experiments, atmospheric CO_2 concentration has decreased to approximately 10% of its initial value after 10 kyr across the different emission scenarios (Fig. 12c). Our values are on the
360   lower end of the range provided by Archer et al. (2009a) due to the combined effect of a higher pre-industrial weathering rate and stronger weathering feedbacks. After 100 kyr from the start of the REF experiments, the fraction of emissions remaining is on average 4.3% (range 4.0–4.4%) across the different emission scenarios (Fig. 12a). This falls in between estimates by
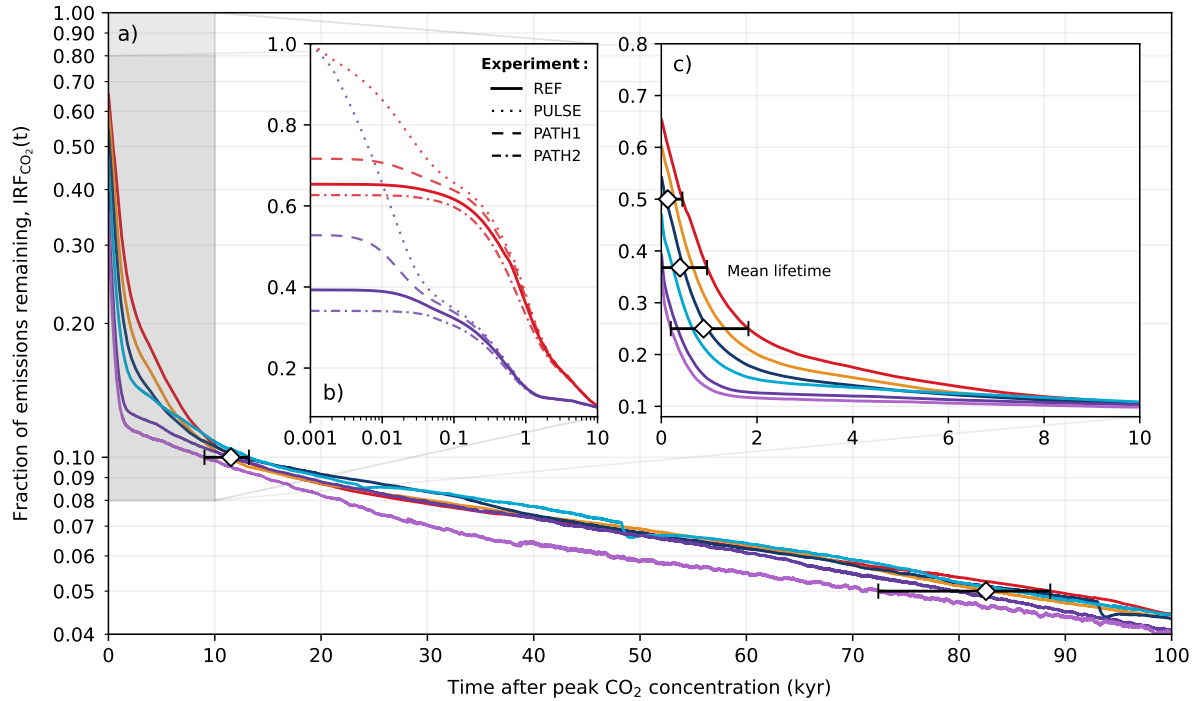
Figure 12. Atmospheric lifetime of anthropogenic CO_2 **described by** $\mathbf{IRF}_{CO_2}(\mathbf{t})$**.** Colours correspond to the cumulative emission scenarios shown in Fig. 2. (a) Fraction of emissions remaining in the atmosphere over the course of 100 kyr for the different emission scenarios in the REF experiment. (b) Fraction of emissions remaining in the atmosphere over the first 10 kyr after peak CO_2 concentration. Here, the x-axis is log-scaled, and only shows the 1000 PgC (purple) and 5000 PgC (red) scenarios. The PULSE, PATH1 and PATH2 experiments have additionally been plotted to show the effect of the emissions pathway on the IRF. (c) Same as (a), but for first 10 kyr after peak CO_2 concentration. The diamond markers and horizontal bars represent the mean time and spread in which the different emission scenarios reach 50%, ≈1/e% (mean lifetime), 25%, 10% and 5% of its original cumulative emission.

previous studies, which have reported that between 2–7% of emissions will remain in the atmosphere beyond 100 kyr (Archer, 2005; Lenton and Britton, 2006; Jeltsch-Thömmes and Joos, 2020).

3.3 Multi-exponential timescale analysis

We conducted a least-squares fit of a multi-exponential decay function to tease out different timescales which can be otherwise associated with long-term processes that take up excess CO_2. This analysis was exclusively done on the REF experiment, the experiment with a pulse-like perturbation of CO_2 (PULSE, Table 1), and the experiment with land carbon disabled (noLAND, Table 1). The latter two experiments were included to (1) provide confidence in our estimated timescales by excluding the ramp up period of emissions as a factor (aligning with the procedure used in similar studies, e.g., Archer et al., 1997), and (2)

facilitate a direct comparison with the findings of Lord et al. (2015b). The Python function *curve_fit* in *Scipy.Optimize* was used, employing nonlinear least squares to fit the following function to our data:

$$CO_2(t) = 280 + \Delta CO_2^{max} \sum_{i=1}^{n} A_i \cdot exp\left(-\frac{t}{\tau_i}\right) \qquad (5)$$

375

where $CO_2(t)$ is the CO_2 concentration at time t (where $CO_2(t_0) = CO_2^{max}$), and ΔCO_2^{max} is peak CO_2 concentration compared to pre-industrial concentration (280 ppm). This function represents the superposition of exponential decay functions each with their own time constant, τ_i, and amplitude, A_i (Maier-Reimer and Hasselmann, 1987). Here, the former represents the timescale of decay (i.e., the removal timescale), and the latter represents the fraction of emissions removed over that timescale.

380 Since an instantaneous emission pulse was not used in the REF and noLAND experiments, the first ∼200 years of our simulations were dedicated to the ramp up and ramp down of atmospheric CO_2 concentration (Fig. E2). Therefore, we decided to fit all data starting from peak concentration in atmospheric CO_2 (as done in Section 3.2), thereby omitting the ramp up period of emissions. Several superimposed exponential functions were used to fit the data (from n=1 to 6), but fast convergence times and significantly high (>0.97) R^2-values were found for n = 3.

385 We should first highlight that it is not surprising that n = 3 yielded a good fit across the different experiments. Although the equilibrium timescales for "fast" carbon processes have been thoroughly examined in previous literature (e.g., Eby et al., 2009), Archer and Brovkin (2008) outlined that long-term carbon uptake would be predominately controlled by the slow processes of (1) ocean invasion, (2) reactions with $CaCO_3$, and (3) reactions with igneous (i.e., silicate) rocks. In some studies, these are sometimes more broadly grouped into "ocean" and "geological" processes, with $CaCO_3$ reactions further split into sea floor

390 and terrestrial $CaCO_3$ neutralization (corresponding to n = 4, e.g., Archer et al., 1997). Other studies have used higher orders of n to account for (or further break down) processes related to land carbon, air–sea CO_2 exchange, ocean invasion/carbonate chemistry, mixed-layer mixing, and deep ocean mixing (Colbourn et al., 2015; Lord et al., 2015b; Jeltsch-Thömmes and Joos, 2020). However, short-term processes (sub-centennial timescales) cannot be fit with our analysis after removing the ramp up period of emissions, meaning n = 3 is already sufficient for examining the long-term uptake of anthropogenic CO_2. It should be

395 noted that, due to this, the values for A_i in the REF and noLAND experiments do not sum to 1 as a fraction of emissions was already removed via short-term processes (Fig 12b). In the REF experiment, removal timescales of 386–810 years for i = 1, ∼4–17 kyr for i = 2, and ∼108–159 kyr for i = 3 were found across the different emission scenarios (Table E2). The estimated range of removal timescales marginally changes for the PULSE and noLAND experiments (Table E2).

The centennial magnitude of the first removal timescale (i = 1) suggests the involvement of ocean circulation, which we

400 interpret as deep ocean processes responsible for transporting CO_2 away from the surface. The range determined in the REF, PULSE, and noLAND experiments fit well within previous estimates: for example, Archer et al. (2009a) found a range of 250–450 years, while Lord et al. (2015b) found 230-880 years. The ability of this process to remove carbon with increasing emissions is nonlinear, as the fraction of emissions removed steadily increases until ∼3000–4000 PgC cumulative emissions
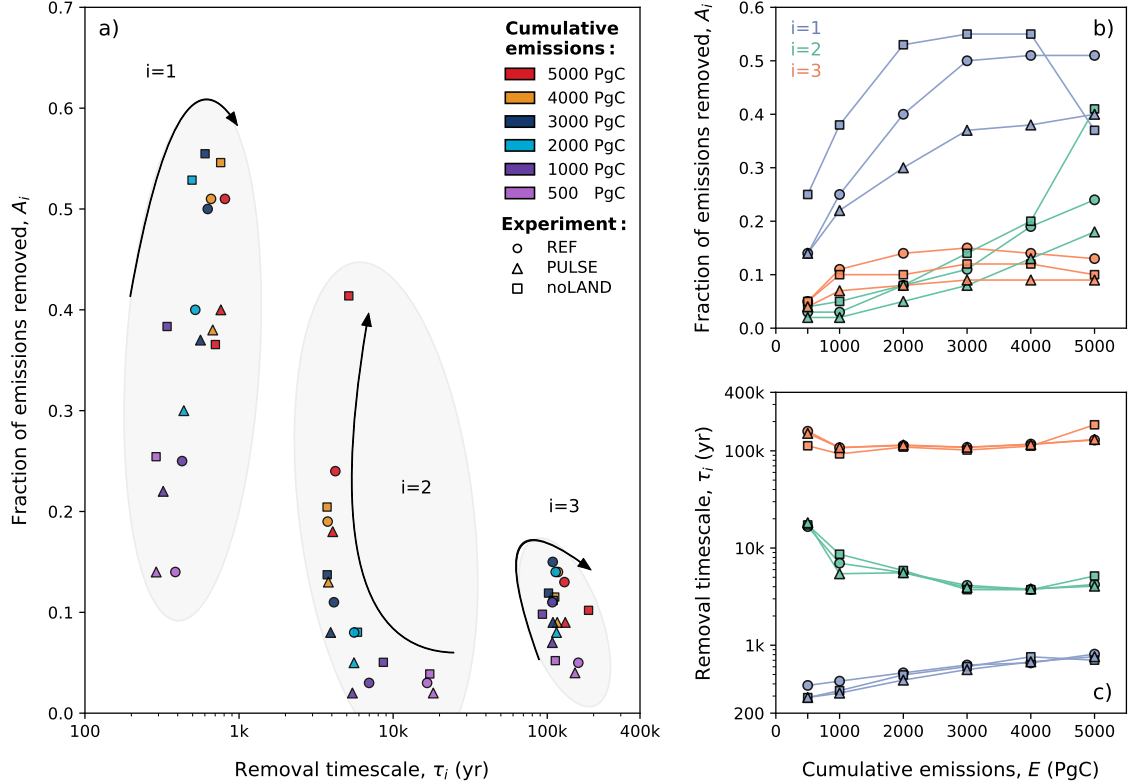
Figure 13. Dependence of fitting parameters (A_i **and** τ_i) **as determined in the multi-exponential decay analysis of** CO_2 **concentration in the REF, PULSE, and noLAND experiments.** Different markers have been used to convey different experiments. The arrows in (a) indicate how the ability of individual processes to remove anthropogenic CO_2 change as total emissions increase. This is shown more explicitly in (b) and (c), which depicts how the fraction of emissions remaining and the removal timescales for different processes change with increasing emissions. Scenarios with smaller cumulative emissions typically result in lower A_i values, as a larger proportion of emissions is taken up by short-term processes (sub-centennial timescales), which are not considered in our multi-exponential fitting procedure (see Lord et al., 2015b).

(Fig. 13b). A major cause of this behaviour is the slowdown of ocean circulation during the first millennium, as seen by the weakening of AMOC. In our experiments, both the duration and magnitude of AMOC weakening increases with larger cumulative emissions (Fig. 7e), followed by a subsequent strengthening of the AMOC after emissions cease, which overshoots the pre-industrial value. This promotes the downward transport of anthropogenic carbon and therefore increases the oceanic carbon uptake capacity (Montenegro et al., 2007; Lord et al., 2015b). In the 5000 PgC scenario, however, the behaviour of this timescale differs significantly between the three experiments (Fig. 13). While deep ocean processes in the REF (and to some extent, in the PULSE) experiment stabilize at a similar removal capacity as in the 4000 PgC scenario (Table E2), its ability is notably reduced in the noLAND experiment ($\sim$37%). In the REF experiment, AMOC does not begin recovery until 200–300 years after emissions end in the 5000 PgC scenario (Fig. 7e), leading to large amount of anthropogenic carbon accumulating in the upper ocean by 1 kyr (Fig. E3). However, AMOC eventually recovers and follows a similar trajectory to that of the 4000 PgC experiment. This is also true for the PULSE experiment, although not shown. Meanwhile, AMOC fails to recover with 5000 PgC in the noLAND experiment, shutting down for the majority of the simulation (not shown). This results in the decreased ability of deep ocean processes to absorb additional anthropogenic CO_2.

Previous studies have given a range of 1–6 kyr for sediment dissolution, and 6–14 kyr for carbonate weathering (Sundquist, 1991; Archer et al., 1997; Ridgwell and Hargreaves, 2007; Colbourn et al., 2015; Lord et al., 2015b; Jeltsch-Thömmes and Joos, 2020). However, it has been emphasized that these processes should not be considered separately given their interdependence (Lord et al., 2015b). We attribute the second calculated timescale (i = 2), which is similar in all three experiments and falls within the estimated range, to the combined influence of both processes. As emissions increase to 4000 PgC, the removal timescale shortens (Fig. 13c), and a higher fraction of emissions is removed (Fig. 13b). The enhanced ability of this timescale to remove anthropogenic CO_2 with larger cumulative emissions is primarily driven by the resulting increase in carbonate weathering, which leads to more HCO_3^- in the ocean (Fig. 9a). In low emission scenarios, the calculated removal timescale is closer to $\sim$17 kyr, suggesting that terrestrial weathering of carbonate rocks is the dominant process of carbon removal. But considering that this timescale generally has a limited capacity to remove additional anthropogenic CO_2 ($\sim$3-4% in the REF experiment, Table E2), it suggests that the combined effect of enhanced carbonate weathering (Fig. 9a) and $CaCO_3$ dissolution (Fig. 8e) is relatively weak in low emission scenarios.

In high emission scenarios, however, the timescale shortens to about 4 kyr; closer to that which is estimated for marine sediment dissolution. Sediment dissolution from a shoaling lysocline and CCD in the 3000-5000 PgC scenarios reach a similar maximum of $\sim$0.17 PgC yr^{-1} shortly after the first millennium in the REF experiment (Fig. 8e). As this process restores buffering capacity to the ocean, and is responsible for the continued removal of anthropogenic CO_2, it is perhaps not so surprising that there is a discernible threshold in the removal timescale at these levels of emissions. Again, the removal ability of this timescale in the 5000 PgC scenario differs significantly between the REF, PULSE, and noLAND experiments. This scenario in the noLAND ensemble accounts for the removal of nearly twice as much anthropogenic CO_2 compared to the other two (41% vs. 18 and 24%). This shows that a weakening ability of deep ocean processes to take up CO_2 is compensated by an increasing ability of sediment dissolution, to some extent (similarly shown in Archer et al., 1997), and is because

seafloor $CaCO_3$ neutralization will act to restore buffering capacity that has been depleted from highly alkaline deep water (Fig. E4c,g,k).

440   The last timescale to be considered (i = 3) pertains to silicate weathering. The multi-exponential analysis shown here provides an estimate on the silicate weathering timescale which is significantly shorter than what has been previously reported. For the first time, a non-monotonous dependence of the silicate weathering timescale and capacity for carbon removal to cumulative emissions is found. This trend is seen in the REF, PULSE, and noLAND experiments, although the spread of the timescale significantly changes between the different experiments. In the 500 PgC scenario, silicate weathering is responsible

445   for removing ∼4-5% of anthropogenic CO_2 across the different experiments (Table E2). However, the removal timescale is approximately 159 kyr in the REF experiment, 151 kyr in the PULSE experiment, and 113 kyr in the noLAND experiment – the latter nearly a factor 2 less than originally estimated by Archer et al. (1997), Colbourn et al. (2015), and Lord et al. (2015b). The ability of this process to remove carbon increases up to a maximum of 15% (seen in the REF experiment) as emissions increase. At the same time, the removal timescale of silicate weathering in the REF experiment decreases to ∼107 kyr in the

450   1000 PgC scenario, before generally increasing to ∼129 kyr in the 5000 PgC scenario (Fig. 13c). This trend can also be seen in the PULSE and noLAND experiments (Fig. 13c). The initial shortening of the silicate weathering timescale with increasing emissions can be partially explained by spatially explicit weathering (Colbourn et al., 2013), and strong weathering feedbacks (Section 3.1). This is not unexpected given that differences in weathering parametrizations have been found to change the estimated timescale of silicate weathering by more than 100 kyr (Uchikawa and Zeebe, 2008; Colbourn et al., 2015).

455   The behaviour of the silicate weathering timescale mirrors that of $CaCO_3$ reactions, as the timescale generally decreases as emissions rise until approximately 3000–4000 PgC (Fig. 13c). The threshold of ∼3000–4000 PgC is also seen for deep ocean processes, which increase in removal ability until that point (Fig. 13b). The non-monotonic behaviour of the silicate weathering timescale and carbon removal ability can be attributed to the same physical mechanisms responsible for the nonlinearity observed in deep ocean processes and $CaCO_3$ reactions. If removal by either of these processes is strong, it can diminish the

460   effectiveness of silicate weathering by reducing the amount of atmospheric CO_2 available for it to act upon. As such, AMOC likely plays a significant role in the removal timescale of silicate weathering, as experiments with a delayed AMOC recovery (Fig. 7e), or a complete shutdown (not shown), show an increase in the timescale. Since emission scenarios greater than 5000 PgC were not explored, it is unclear whether this trend will continue with increasing emissions. Despite differences in our estimated timescale of silicate weathering, the ability of silicate weathering to remove carbon (∼4–15% across all experiments

465   and scenarios, Table E2) falls reasonably close to previous studies, which has reported values between 4–10% (Lenton and Britton, 2006; Ridgwell and Hargreaves, 2007; Archer, 2005; Colbourn et al., 2015; Lord et al., 2015b).

3.4   Continuum of removal timescales

The multi-exponential decomposition of atmospheric CO_2 (Section 3.3), is, to some extent, dependent on how well a discrete number of functions can describe the continuous decline in atmospheric CO_2. This drawback has been recognized and dis-

470   cussed by other studies (e.g., Jeltsch-Thömmes and Joos, 2020). Therefore, we have derived an alternative method to calculate the removal timescale of anthropogenic CO_2 emissions as a function of time. With this method, the following first-order ex-

ponential decay equation describing the decline of atmospheric CO_2 (Eq. 6) is solved to estimate the removal timescale, $\tau(t)$. This was done by estimating the derivative using a central difference approach:

$$\frac{d\Delta CO_2(t)}{dt} = \frac{-\Delta CO_2(t)}{\tau(t)} \qquad (6)$$

475

$$\tau(t) = \frac{-2\Delta t \Delta CO_2(t)}{\Delta CO_2(t+\Delta t) - \Delta CO_2(t-\Delta t)} \qquad (7)$$

where $\Delta CO_2(t)$ is the change in atmospheric CO_2 concentration at time t (where $CO_2(t_0) = CO_2^{max}$) compared to the pre-industrial concentration (280 ppm). In doing this, the time-dependence of the calculated removal timescales could be examined,

480 along with how it changes for different levels of cumulative CO_2 emissions. We employed a rolling mean with an increasing window size over time, such that larger removal timescales are averaged over longer time periods. This has been more thoroughly described in Appendix D. Like Sections 3.2 and 3.3, the ramp up period of emissions was excluded, meaning that this analysis was carried out for data after peak CO_2 concentration had been reached ($CO_2(t_0) = CO_2^{max}$). This method was conducted exclusively on the REF experiment, as one of its objectives was to provide greater confidence in the results obtained

485 from Section 3.3.

The calculated removal timescale for the REF experiments are shown in Fig. 14a. As expected, the removal timescale is generally short in the beginning. At peak CO_2 concentrations, the estimated removal timescale ranges between $\sim$0.3–1.6 kyr in the REF experiment (Fig. 14a). Between 1–10 kyr, there is a period in time in which removal timescale temporarily increases for the 500 and 1000 PgC scenarios (Fig. 14a). This behaviour in removal timescales is due to multi-millennial processes at

490 this time which temporarily stabilize atmospheric CO_2 concentrations (since $\tau(t) \propto \left(\frac{dCO_2(t)}{dt}\right)^{-1}$). As this occurs around the same time as when $CaCO_3$ reactions are particularly significant for the removal of anthropogenic CO_2 (Fig. 13), it is likely related to the weak, combined effect of deep-sea carbonate dissolution and terrestrial weathering in these scenarios (discussed in Section 3.3). At 50 kyr, the effect of carbonate weathering becomes minimal and the removal timescale primarily reflects silicate weathering. Interestingly, the removal timescale for the $\sim$1000–4000 PgC scenarios converge to a value lower than

495 that in the 500 and 5000 PgC scenarios (Fig. 14b). This generally confirms that the non-monotonic behaviour of the silicate weathering timescale seen in the multi-exponential analysis (Fig. 13) is not just an artifact of the fit. Averaging over the last 5,000 years of $\tau(t)$ yields a mean removal timescale of approximately 89 kyr for the REF experiment (range 80–105 kyr, Fig. 14b). This method generally provides estimates on the silicate weathering timescale that are slightly lower and exhibit less spread compared to those obtained in Section 3.3. The multi-exponential analysis is helpful for understanding the role and

500 removal ability of each process individually. However, this second method provides more confidence in calculating the silicate weathering timescale, as it is not influenced by factors such as the number of superimposed exponential functions (n), or the goodness of fit.
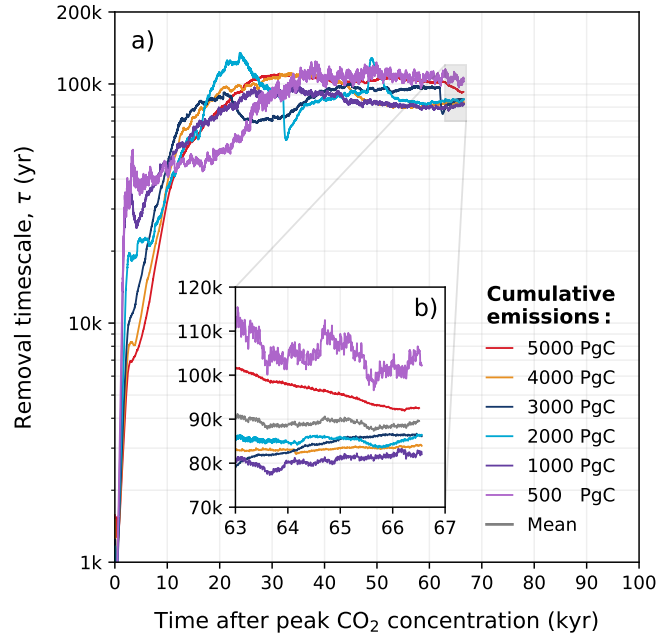
Figure 14. Estimated removal timescale τ at any given time as determined from Eq. 7 for the different emission scenarios in the REF experiment. Data has been filtered with the variable moving window discussed in Appendix D for visibility, and is why the estimated removal timescale is not available for the full 100 kyr.

4 Sensitivity experiments

To explore the sensitivity of our results to different carbon cycle processes and climate sensitivity, we have performed a
505 number of additional experiments (Table 1). The results from these additional experiments are discussed below. To provide a linear analysis of our sensitivity experiments, we limit our emission scenarios to ≤3000 PgC. This is largely because high levels of cumulative emissions make it difficult to ignore secondary and cascading effects (e.g., shutdown of AMOC), which would introduce nonlinearities and provide additional uncertainties.

4.1 Land carbon sink

510 A complete disregard of the land carbon pool results in higher atmospheric CO_2 concentrations at the start of our simulations (Fig. 15a). Peak atmospheric CO_2 concentrations are between ∼65-340 ppm higher without the land carbon pool, depending on the emission scenario. These peak magnitudes generally align with previous modelling work without a land carbon pool (Lord et al., 2015b; Köhler, 2020). After peak CO_2, the difference in atmospheric CO_2 concentrations between the noLAND and REF experiments begins to decrease for all emission scenarios up to 3000 PgC. Conversely, carbon inventory of the ocean
515 increases to approximately 2300 PgC by 1 kyr, which is roughly 300 PgC more than in the REF experiment (Fig. 16d). The majority of this carbon uptake in the ocean occurs at peak CO_2 concentration from increased air–sea CO_2 flux. However, at
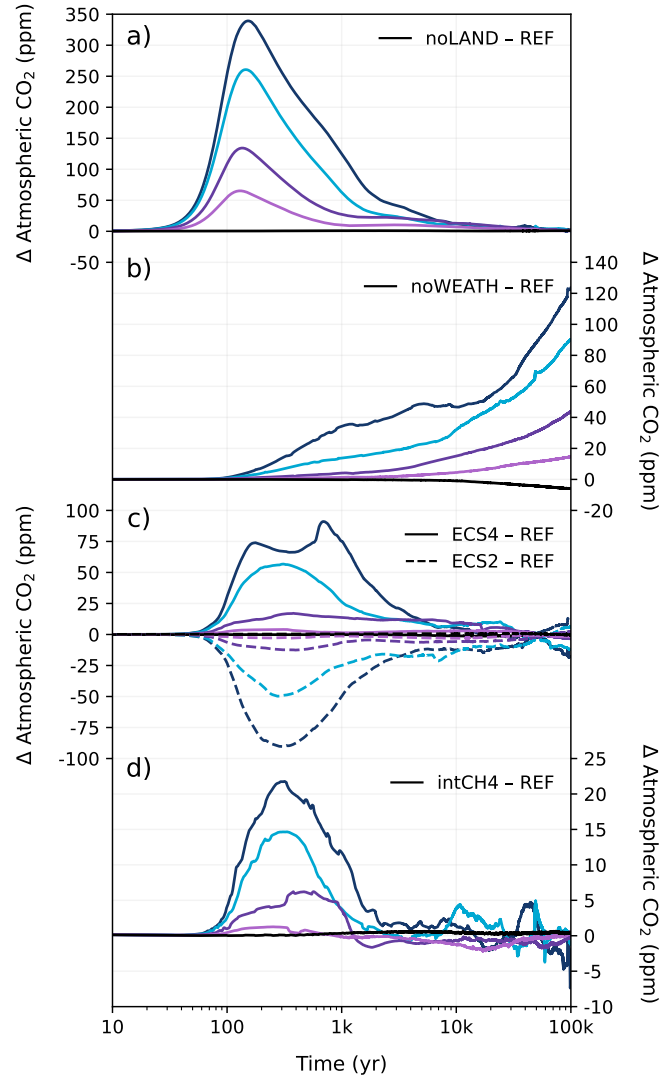
Figure 15. Difference in atmospheric CO_2 **concentration in the different sensitivity experiments compared to the REF experiment.**
(a) The effect of disabling the land carbon pool. (b) The effect of constant weathering (i.e., removal of the weathering feedback). (c) The effect of a lower (2 °C) and a higher (4 °C) equilibrium climate sensitivity compared to the standard 3.1 °C in CLIMBER-X. (d) The effect of interactive methane. Negative anomaly values represent a larger atmospheric concentration in the REF experiment. Colours correspond to the cumulative emission scenarios shown in Fig. 2.

least some of this carbon is from sediment dissolution (Fig. 16g), which contributes approximately 50 PgC more by 1 kyr. At the beginning of the noLAND experiment, less CO_2 is absorbed as a whole, as it is taken up by relatively slow ocean and weathering processes. This leads to a higher fraction of emissions remaining in the atmosphere compared to the REF experiment (Fig. 17a).

It has long been recognized that land plays a crucial role in modulating the effects of weathering (Nugent and Matthews, 2012; Brault et al., 2017). However, the influence of land carbon on the long-term removal of anthropogenic CO_2 through silicate weathering remains largely understudied. Since atmospheric CO_2 concentrations are higher in the noLAND experiment (Fig. 15a), peak temperatures and runoff are also elevated. As weathering in CLIMBER-X is driven by changes in runoff and temperature (see Eq. 2 and 3), the noLAND experiment produces higher weathering fluxes compared to the REF experiment. This leads to a faster decline of atmospheric CO_2 concentrations in the long term and a shorter silicate weathering timescale. Averaging over the last 5,000 years of $\tau(t)$ in Fig. 17b yields an average value of approximately 79 kyr for the noLAND experiment. By 100 kyr, when silicate weathering becomes the dominant carbon removal process, the higher silicate weathering in the noLAND experiment brings atmospheric CO_2 concentrations closer to those in the REF experiment (Fig. 15a). As a result, the average fraction of emissions remaining between the REF and noLAND experiments differ by only 0.2% at this time (Fig. 17a). The higher weathering in the noLAND experiment therefore partially compensates both higher initial atmospheric CO_2 concentrations and a missing land carbon pool on long timescales.

4.2 Silicate weathering feedback

In the absence of a silicate weathering feedback, atmospheric CO_2 concentrations cannot be restored back to pre-industrial conditions (Fig. 17a). Initially, atmospheric CO_2 concentrations are quite similar between the REF and noWEATH experiments, as weathering is only responsible for taking up approximately 3% of anthropogenic CO_2 within the first 1 kyr after emissions end (Fig. 3). However, the two experiments quickly diverge as atmospheric CO_2 is additionally consumed by enhanced weathering in the REF experiment. The difference in atmospheric CO_2 concentration between the REF and noWEATH grows to ~120 ppm over the course of 100 kyr (Fig. 15). This is because the value to which atmospheric CO_2 concentrations returns to in the noWEATH experiments increases with larger emissions (with final values between ~300–470 ppm compared to the pre-industrial 280 ppm). Across the different emission scenarios, the last ~14% (range 13–15%) of anthropogenic CO_2 in the noWEATH experiment cannot be removed without the weathering feedback (Fig. 17). This estimate is larger than what was calculated for the fraction of emissions removed by the silicate weathering timescale in the noLAND experiment (range 5–12%, Table E2) and range provided by previous studies (range 4–10%; Lenton and Britton, 2006; Ridgwell and Hargreaves, 2007; Archer, 2005; Colbourn et al., 2015; Lord et al., 2015b; Jeltsch-Thömmes and Joos, 2020). As atmospheric CO_2 concentrations do not decrease beyond ~300–470 ppm in the noWEATH experiments, temperatures stay significantly elevated (and near constant) until the end of the simulation. Climate is therefore very different in the noWEATH experiment, resulting in notably different behaviour in the land, ocean, and sediment carbon pools compared to the REF experiment (Fig. 16).
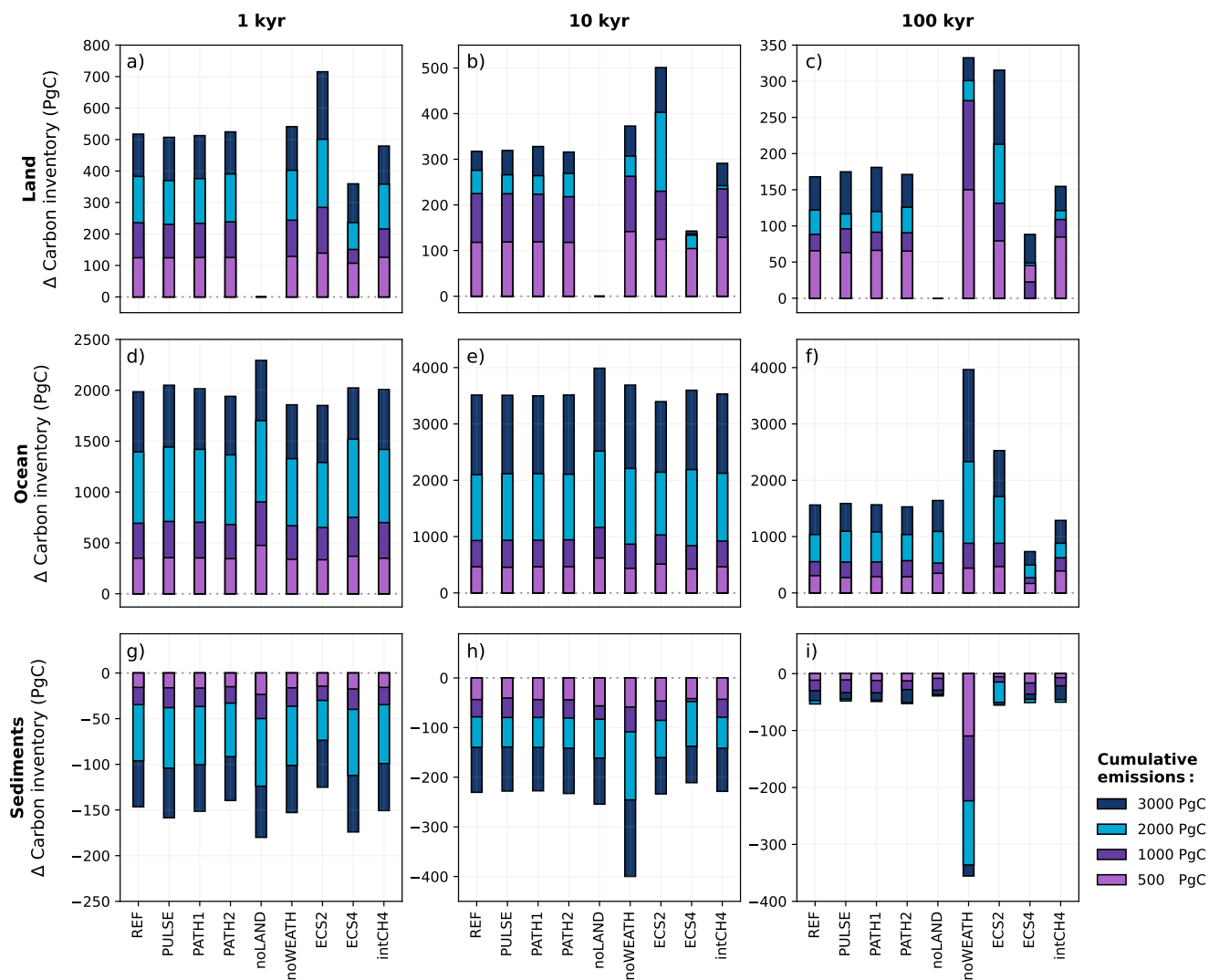
Figure 16. Net cumulative uptake of carbon in the (a-c) land, (d-f) ocean, and (g-i) sediment carbon pools across the different sensitivity experiments and emission scenarios. The stacked bar plot is cumulative, meaning that the height of the bar (rather than the bar length) in each emission scenario reflects the magnitude of carbon uptake or loss. Positive values represents carbon into the land, ocean and sediment carbon pools. The time slices of (a,d,g) 1 kyr, (b,e,h) 10 kyr, and (c,f,i) 100 kyr were chosen to capture the effects of the different timescales. It should be noted that the time slices here are measured from the start of the simulations, which includes the emissions ramp up period.

4.3 Climate sensitivity

The best estimate of equilibrium climate sensitivity is reported as 3 °C by the IPCC (Canadell et al., 2021), which is close with the estimated ECS of 3.1 °C in CLIMBER-X. However, the IPCC also reports that the very likely range is 2 °C to 5 °C, so the effect of a lower and higher ECS (corresponding to values of 2 °C and 4 °C, Appendix A) was also tested. As seen in Fig. 15c, simulations using a lower ECS produces lower atmospheric concentrations of CO_2 (and vice versa), and higher levels of cumulative emissions produce larger differences from the REF experiment. The differences in atmospheric CO_2 concentration can largely be traced back to changes in land carbon inventory (Fig. 16a). In the case of ECS4, terrestrial vegetation takes up approximately the same amount of carbon as in the REF experiment (not shown). However, increased warming causes soil carbon to become a larger source of carbon, resulting in higher atmospheric CO_2 concentrations and lower land carbon across the different emission scenarios over the 100 kyr. This behaviour is indicative of a positive feedback as a result of warming-induced soil carbon release. For ECS2, the storage of anthropogenic CO_2 in the vegetation and soil carbon pools are positive for the entire duration of the simulation regardless of the emission scenario (not shown). Despite significant variations in the partitioning of carbon between the land and ocean carbon pools (Fig. 16), differences in atmospheric CO_2 concentration between the ECS2/ECS4 experiments and the REF experiment are within ∼5 ppm by 10 kyr, and remain low for the rest of the simulation (Fig. 15c).

At first glance, this might suggest that the impact of ECS on atmospheric CO_2 concentration is minimal after 10 kyr regardless of the cumulative emission scenario. This behaviour was similarly seen in Shaffer et al. (2009). However, this conclusion is only valid for a short period. In Fig. 17c,d, higher ECS values leads to a faster decline in atmospheric concentration and a shorter removal timescale of silicate weathering. Although atmospheric CO_2 concentrations are initially higher in the ECS4 experiment, they fall below those of the REF experiment around 50 kyr due to substantial consumption by weathering (Fig. 15c). The reverse is true for ECS2. Averaging over the last 5,000 years for $\tau(t)$ results in a mean silicate weathering timescale of 153 kyr for an ECS of 2 °C, and 54 kyr for an ECS of 4 °C. This generally corroborates findings by Colbourn et al. (2015), who found that a lower ECS would give a longer timescale for silicate weathering. With that in mind, the default ECS in Colbourn et al. (2015) and Lord et al. (2015b) was 2.64 °C, indicating that climate sensitivity could account for at least some of the differences in our estimated silicate weathering timescale (Fig. 13).

4.4 Interactive methane

Global warming from anthropogenic CO_2 emissions can cause additional methane emissions from natural sources that can result in an additional positive feedback loop. Although methane has a relatively short atmospheric lifetime compared to our experiment duration (∼9.8 years, Voulgarakis et al., 2013), it has a higher global warming potential compared to CO_2. An increase in methane concentration could therefore affect the capacity of different Earth system components to take up carbon over time. For the first time, we investigate the impact of interactive methane on the long-term carbon cycle. A simple methane cycle has been implemented in CLIMBER-X that explicitly simulates the natural methane emissions from land resulting from anaerobic respiration in wetlands and peatlands (Willeit and Ganopolski, 2016). Permafrost is treated in the methane model
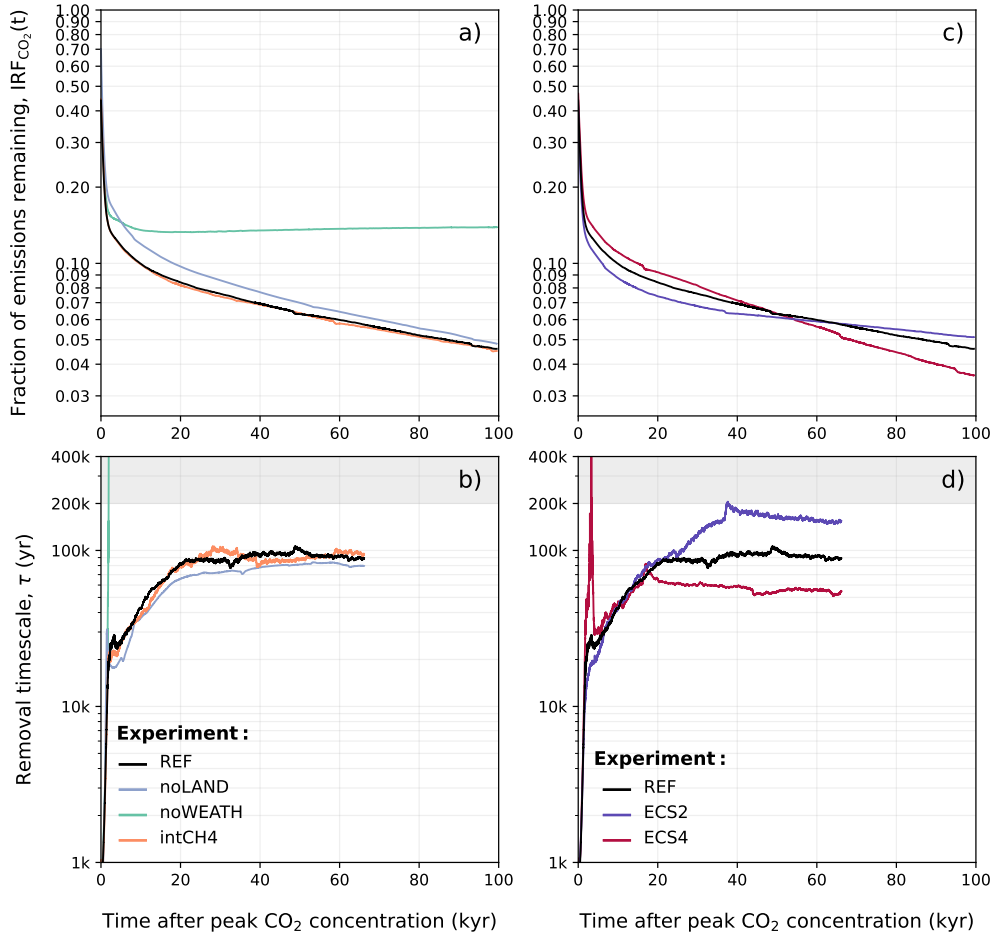
Figure 17. Comparison of (a,c) the atmospheric lifetime of anthropogenic CO_2 **described by IRF$_{CO_2}$(t) and (b,d) removal timescale of anthropogenic** CO_2 **in the different sensitivity experiments.** The mean of the 500-3000 PgC scenarios is shown. As described in Sections 3.2 and 3.4, the emissions ramp up period was excluded from the calculation of IRF$_{CO_2}$(t) and τ(t). Data in (b,d) has been filtered with the variable moving window discussed in Appendix D for visibility, and is why the estimated removal timescale is not available for the full 100 kyr.

through the representation of anaerobic decomposition in saturated soils – a process that can take place in permafrost regions. Atmospheric methane concentration is then computed assuming a constant atmospheric lifetime of methane (Willeit et al., 2023).

585   In the zero emissions scenario, CH_4 concentration stays largely around 600–700 ppb (close to the constant 600 ppb set in the REF experiment, Fig. E7b). For the other scenarios (500–3000 PgC), atmospheric CH_4 concentrations rise over the first ~200 years, reaching a peak of approximately 1620 ppb in the 3000 PgC experiment. With interactive methane, atmospheric CO_2 concentrations can be up to 20 ppm higher than in the REF experiment (Fig. 15d). During much of the first 1 kyr, the difference in atmospheric CO_2 concentration between the intCH4 and REF experiments increase with higher emissions.

590   However, this pattern changes as atmospheric CO_2 concentrations decline, and does not hold beyond the first 1 kyr. Global mean temperature in the 3000 PgC scenario is up to 0.5°C higher in the intCH4 experiment (Fig. E7a), but the difference remains largely negligible in the low emission scenarios. While total vegetation carbon is similar between the REF and intCH4 experiments, soil carbon in the intCH4 experiments is notably lower across the different emission scenarios, causing the land carbon pool to take up less than the REF experiment overall (Fig. 16a-c). Carbon stored in peatland is responsible for some of

595   these differences, as carbon is lost from warming-induced soil respiration. Beyond the first 5 kyr, interactive methane has a ±5 ppm effect on atmospheric CO_2 concentration (Fig. 15d). Temperature differences between the intCH4 and REF experiments also tend to decrease around this time, and despite small variations in how temperature evolves, the experiments largely follow each other for the rest of the simulation (Fig. E7a). In this way, the lifetime of anthropogenic CO_2 and removal timescales in the intCH4 experiments do not differ significantly from the REF experiment over long timescales (Fig. 17a,b), suggesting that

600   the indirect effect of CH_4 on the climate (through CO_2) is likely negligible over such periods.

5   Discussion and conclusions

The impacts of anthropogenic climate change will likely be felt for tens of thousands of years, if not hundreds of thousands of years – long after the anthropogenic emission of CO_2. By simulating the long-term response to idealized emission scenarios, we highlighted how processes that remove carbon from the atmosphere change with different levels of cumulative emissions. With

605   this, we have examined the capacity and extent of these processes to take up carbon on different timescales. To some extent, the results of this study align with previous investigations. For example, we have shown that the magnitude of cumulative emissions will predominantly control the long-term response, supporting the path independence found by previous work (Matthews et al., 2009; Zickfeld et al., 2012; Herrington and Zickfeld, 2014). The decline in anthropogenic CO_2 over time seen here generally falls within estimates given by the multi-model assessment in Archer et al. (2009a) and other studies: approximately 10%

610   of anthropogenic emissions will persist longer than 10,000 years, and ~4% beyond 100,000 years. The response of deep ocean processes and $CaCO_3$ reactions, as well as their ability to remove anthropogenic CO_2 at different levels of cumulative emissions, also supports earlier investigations (Lord et al., 2015b). However, the extensive sensitivity analysis, along with the higher resolution and complexity of CLIMBER-X, have lead to several new findings:

The removal timescale of silicate weathering is significantly influenced by a number of factors. In this study, we quantified the effects of climate sensitivity, the land carbon pool, weathering feedbacks, and dynamically changing methane concentrations on the atmospheric lifetime of anthropogenic CO_2. The sensitivity analysis revealed that climate sensitivity has the most significant influence on the silicate weathering timescale (Fig. 17). However, most factors were generally found to impact the silicate weathering timescale, albeit in inverse ways. Our results show that a higher climate sensitivity, stronger silicate weathering feedbacks, a spatially explicit weathering scheme, and no land carbon pool reduces the removal timescale of silicate weathering, whereas a lower climate sensitivity and a land carbon pool increases this timescale. This means that, in theory, the same silicate weathering timescale could be obtained with no land carbon and either weaker weathering feedbacks/lower ECS. This emphasizes the importance of incorporating as many components of the carbon cycle as possible, and increasing model complexity in Earth system models as to more accurately represent the long-term future behaviour of atmospheric CO_2. Furthermore, the global heterogeneity of carbonate and silicate weathering with increasing emissions (Fig. 11) also showed the importance of highly active weathering regions to the global weathering flux (Section 3.1.3), highlighting the need for spatially explicit schemes. Improving the silicate weathering timescale would require more accurate constraints on both these factors and the global silicate weathering flux, and a deeper understanding of how weathering responds to increasing global temperatures.

The removal timescale of silicate weathering is significantly shorter than previously estimated. The two methods used in this study provided significantly shorter removal timescales for silicate weathering compared to previous research, providing a best estimate of 80–105 kyrs depending on the emission size. This discrepancy is likely due to differences in climate sensitivity, weathering feedbacks, a spatially explicit weathering scheme and a land carbon pool. With this in mind, our estimates here do not address (potentially large) uncertainties related to the sensitivity of silicate weathering processes such as erosion limitation or net primary production on land. Nevertheless, it is worth noting that ∼20-30 years has passed since the constant 200-400 kyr range was first established for the silicate weathering timescale using lower complexity models (Sundquist, 1991; Archer et al., 1997, 1998), and our results indicate that it is time to re-examine this estimate. Considering the large uncertainty that exists in the literature concerning its value, and progress made in model resolution and process descriptions since the last LTMIP both in our model and others, another intercomparison project could be beneficial.

The removal timescale of silicate weathering is dependent on the magnitude of cumulative emissions. A major finding in Lord et al. (2015b) was that the removal ability and timescale of silicate weathering was approximately invariant with respect to cumulative emissions. This is challenged here, as it was shown that both are non-monotonous with increasing emissions. In all experiments which were analyzed (REF, PULSE, and noLAND), there is an initial shortening of the silicate weathering timescale with increasing cumulative emissions until ∼3000-4000 PgC. For the 5000 PgC scenario, however, it was found (via two methods) that the timescale increases. Whether this trend persists for emissions beyond 5000 PgC remains to be determined. Future research would benefit from exploring the connection between extended AMOC decline and the long-term removal of anthropogenic CO_2 via silicate weathering.

Land carbon has a significant long-term influence on the future evolution of atmospheric CO_2. Despite variations in vegetation and soil carbon response with increasing emissions, the terrestrial storage of anthropogenic carbon is positive for the

duration of our simulations, and is responsible for storing approximately 4–13% of anthropogenic carbon by the end of the simulation. The land's capacity to absorb anthropogenic CO_2 in the simulations buffers higher CO_2 concentrations and, therefore, peak global temperatures. As a consequence, the inclusion of land carbon cycle processes effectively reduces weathering fluxes, thereby increasing the removal timescale of silicate weathering. Experiments that exclude land carbon would show a shorter silicate weathering timescale than those that include land carbon. As silicate weathering is the ultimate control on the removal of anthropogenic CO_2, the extent to which land buffers peak temperature in a model can significantly influence the atmospheric lifetime of anthropogenic CO_2.

The methane cycle will likely have a negligible effect on long timescales. Rising global temperatures will increase methane levels, potentially amplifying positive feedbacks and impacting how Earth system components absorb carbon over time. These experiments show that a dynamic methane cycle in CLIMBER-X can contribute up to an additional ∼25 ppm in atmospheric CO_2 concentration. However, this effect is mainly limited to the first millennium after emissions end, and is largely negligible on long timescales. As such, the methane cycle does not contribute to substantially different removal timescales, leading to the same rate of anthropogenic CO_2 removal over time as in the REF experiment.

There are several assumptions in our study which should be considered when generalizing the long-term response of the climate-carbon system. Certain aspects of the carbon cycle in CLIMBER-X are simplified or not considered, as current computational restrictions limit the inclusion of all carbon-cycle processes across all timescales. For example, CLIMBER-X does not consider deep-sea methane hydrates or nitrogen limitation on tropical or boreal forests, despite their potential impacts on future carbon uptake (Archer et al., 2009b; Norby et al., 2010). Some general uncertainties and poor empirical constraints should also be considered, as they can inhibit an accurate description of some processes. One such example is the strength of the biological pump in a warming world. Although state-of-the-art Earth system models do not agree on the overall response of marine primary production to increasing CO_2 levels on centennial timescales (Laufkötter et al., 2015), widespread ocean acidification is still expected to have some influence (Mora et al., 2013). This is not considered in our model, which relies on an extended NPZD (nutrients–phytoplankton–zooplankton–detritus) description, typical for models at this level of complexity. The weathering scheme used in CLIMBER-X is significantly more advanced than in other models of the same class, however, it does not explicitly account for changes in vegetation cover or net primary production. While this could be an important simplification, it is presently unclear to what extent it may affect long-term CO_2 dynamics. As 10% of the land area in our simulations is responsible for more than a third of global silicate weathering fluxes, small changes in the controlling parameters in these areas can also significantly impact total weathering fluxes (Hartmann et al., 2009b). Like many other models, CLIMBER-X also does not account for the potentially significant effect of soil shielding, given the limited quantity of data and ongoing uncertainties regarding its impact. However, there is some evidence to suggest that erosion limitation could weaken the strength of the weathering feedback (Goddéris et al., 2008; Maher and Chamberlain, 2014; Maffre et al., 2023), which may increase the estimated removal timescale of silicate weathering. These limitations highlight potential directions for further work.

Few studies (Lenton and Britton, 2006; Lord et al., 2015b; Köhler, 2020; Couplet et al., 2024) have looked at idealized emission scenarios with more than ∼6000 PgC corresponding to unconventional fossil fuels. This was not considered here,

partially because the potential of unconventional fossil fuels is still speculative, but also because such high levels of cumulative

685 emissions make it difficult to ignore additional changes in the Earth system, such as sea level rise. Simulations in this study were carried out using prescribed present-day ice sheets to maintain consistency with previous research. However, the melting of the Greenland and West Antarctic ice sheets, inevitable in high emission scenarios, can introduce additional feedback mechanisms in the carbon cycle (Wadham et al., 2019). These effects could be significant for the range of emissions considered here. Moreover, significant global warming is expected to trigger the crossing of one (or more) critical thresholds in the Earth system

690 (Lenton et al., 2008; Armstrong McKay et al., 2022; Wunderling et al., 2024), which could affect the long-term capacity of different components to absorb carbon over time. In addition to this, it has been assumed that the pre-industrial global carbon cycle was in equilibrium, such that the silicate weathering feedback will eventually return CO_2 concentrations to 280 ppm after an anthropogenic perturbation in the carbon cycle. This assumption can also be explicitly seen in the zero emissions scenario in Fig. 2. While this is a standard assumption for investigations into the long-term response of the climate-carbon

695 system to perturbations in the carbon cycle, it is perhaps not so appropriate for very long time scales considered in this work. The implications of this assumption will be considered in a forthcoming paper. Future work with the CLIMBER-X model will investigate the long-term effects of anthropogenic CO_2 on the dynamic evolution of Northern Hemisphere ice sheets.

Appendix A: Emulation of different climate sensitivities

Previous studies have implemented straightforward ways to scale ECS (e.g., Colbourn et al., 2015). In CLIMBER-X, different climate sensitivities can be achieved by scaling the equivalent CO_2 in the long-wave radiation scheme in the following way:

$$CO_2^{eq,ecs} = e^{\left(\alpha \ln CO_2^{eq} + (1-\alpha) \ln CO_2^{ref}\right)}, \tag{A1}$$

where α is the scaling coefficient, and $CO_2^{ref} = 280$ ppm. The equivalent CO_2 concentration for radiation is CO_2^{eq}, which also includes the effect of other greenhouse gases (Willeit et al., 2023). It was determined a priori that $\alpha = 0.66$ yielded an ECS of 2 °C, whereas an $\alpha = 1.33$ yielded an ECS of 4 °C. This method has been more extensively applied in Höning et al. (2024) and Kaufhold et al. (2024a). More information about this ECS scaling technique in CLIMBER-X, as well as a comparison of with state-of-the-art Earth system models, can be found in Kaufhold et al. (2024a).

Appendix B: Fraction of cumulative fluxes from the atmosphere

The fraction of the different carbon reservoirs which contribute to the removal of anthropogenic CO_2 over a span of 100 kyr is assessed using Eq. B3. This is similar to calculations for airborne, land-borne, ocean-borne and sediment-borne fractions (Jones et al., 2013; Vakilifard et al., 2022), as the cumulative carbon fluxes of the atmosphere, land, ocean, and weathering are normalized by cumulative anthropogenic emissions, E (PgC). However, we focus strictly on changes in cumulative carbon flux from the atmosphere relative to the pre-industrial, instead of changes in carbon inventory, as our experiments were conducted with an open carbon cycle. From Eq. 1 we get:

$$F_{anth} = \frac{dC_{atm}}{dt} - F_{lnd} - F_{ocn} + F_{weath} - F_{volc}, \tag{B1}$$

which, integrated in time gives:

$$\int_0^t F_{anth} dt = (C_{atm}(t) - C_{atm}(0)) - \int_0^t F_{lnd} dt - \int_0^t F_{ocn} dt + \int_0^t F_{weath} dt - \int_0^t F_{volc} dt. \tag{B2}$$

As we only consider times after the cessation of anthropogenic emissions (i.e., $\int_0^t F_{anth} dt = E$, total cumulative emissions), the equation above becomes:

$$1 = \frac{1}{E} \left((C_{atm}(t) - C_{atm}(0)) - \int_0^t F_{lnd} dt - \int_0^t F_{ocn} dt + \int_0^t \left(F_{weath}^{carb} + F_{weath}^{sil} \right) dt - \int_0^t F_{volc} dt \right) \tag{B3}$$

The individual components seen in Fig. 3 are then computed as follows:

$$\Phi_{atm}(t) = \frac{1}{E} (C_{atm}(t) - C_{atm}(0)) \equiv IRF_{CO_2}(t), \tag{B4}$$

$$\Phi_{lnd}(t) = -\frac{1}{E} \int_0^t F_{lnd} dt, \tag{B5}$$

$$\Phi_{ocn}(t) = -\frac{1}{E} \left(\int_0^t F_{ocn} dt - \int_0^t F_{weath}^{carb} dt \right), \tag{B6}$$

$$\Phi_{weath}^{sil}(t) = \frac{1}{E} \left(\int_0^t F_{weath}^{sil} dt - \int_0^t F_{volc} dt \right). \tag{B7}$$

Fluxes (in PgC yr^{-1}) are relative to the average flux over the reference simulation to account for model drift. We add and subtract F_{weath}^{carb} from F_{ocn} and F_{weath} respectively, as carbonate weathering additionally transfers carbon into the ocean and causes ocean outgassing. Volcanic outgassing, F_{volc}, was additionally subtracted from F_{weath} to isolate silicate weathering consumption.

Appendix C: Calculation of the Revelle factor

The Revelle factor ξ quantifies the ocean's ability to absorb CO_2. It essentially compares the ratio of fractional changes of CO_2 by fractional changes in DIC (Sarmiento and Gruber, 2006), making it a useful metric for assessing the sensitivity of our simulations to anthropogenic CO_2 perturbations (Broecker et al., 1979). Given that there are competing definitions in literature (see: Egleston et al., 2010), we explicitly calculate the Revelle factor in the following way:

$$\xi = \frac{\partial \ln pCO_2}{\partial \ln DIC} \tag{C1}$$

Appendix D: Rolling mean with variable window size

One disadvantage in the formulation for $\tau(t)$ in Section 3.4, is that it is sensitive to small-scale variability and noise in $CO_2(t)$. A simple rolling mean is not sufficient to smooth this, as the removal timescale is expected to increase over time, eventually converging to an $\mathcal{O}(10^{5-6})$ timescale which is representative of silicate weathering. For this reason, we use a forward rolling mean to remove noise on both short and long timescales. While a rolling mean is generally defined with a fixed window size, we modified the standard equation to have a variable window size. This can be written as the following:

$$CO_2(t) = \frac{1}{w(t)} \sum_{i=t}^{t+w(t)} CO_2(i), \quad \text{where } CO_2(t_0) = CO_2^{max} \tag{D1}$$

where $w(t)$ is the window size as a function of time, t is time, $CO_2(t)$ is atmospheric CO_2 concentration at time t, and CO_2^{max} is peak CO_2 concentration. Different functions were tested for $w(t)$, but a following simple, linearly increasing window of $w(t) = 0.5t - 70$ provided the best results, as it still preserved the overall trend on multiple timescales. Given data limitations, the rolling window could not extend beyond 100 kyr due to the forward rolling technique. For this reason, the data is cut around approximately $t \approx 67$ kyr, when the window size becomes approximately $w(t) \approx 33$ kyr, and is why data for the full 100 kyr are not shown in both Fig. 14 and 17b,d.
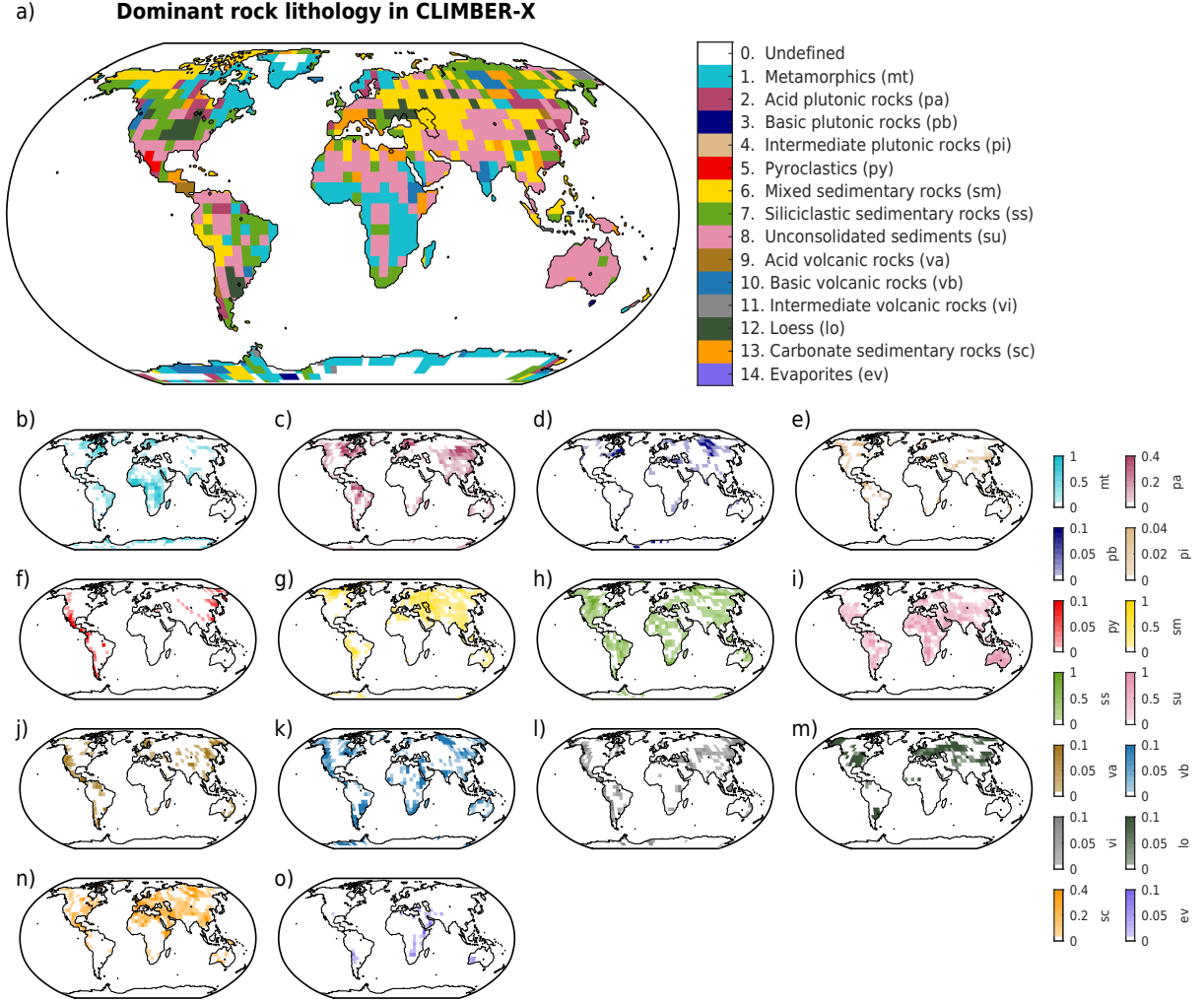
Figure E1. Distribution of the 14 lithological classes implemented in CLIMBER-X for the present day. These are based on the GLiM lithological map (Hartmann and Moosdorf, 2012). The dominant rock type in a given grid-cell is shown in (a). The spatial distribution of grid-cell lithological fractions, $\beta(\ell)$, are given for (b) metamorphic rocks, (c) acid plutonic rocks, (d) basic plutonic rocks, (e) intermediate plutonic rocks, (f) pyroclastics, (g) mixed sedimentary rocks, (h) siliciclastic sedimentary rocks, (i) unconsolidated sediments, (j) acid volcanic rocks, (k) basic volcanic rocks, (l) intermediate volcanic rocks, (m) loess, (n) carbonate sedimentary rocks, and (o) evaporites. Note that the colorbar range for different lithological fractions changes between lithological classes.

Table E1. Lithological classes in CLIMBER-X. These are based on the lithological map of GLiM (Hartmann and Moosdorf, 2012) and their activation energy of silicates is from Hartmann et al. (2014). The evaporites class (ev) is used only to compute phosphorus fluxes in CLIMBER-X, and is therefore also not considered here.

$\ell =$	Lithological Code	Lithological Class	Molality / weathering rate, $b(\ell)$ ($\frac{1}{12} \times$ molC kg^{-1} water)	Activation energy of silicates, $E_{a,sil}(\ell)$ (kJ mol^{-1})	Fraction to weather as carbonate rocks, $\alpha(\ell)$
1	mt	Metamorphics	0.007626	60	0.75
2	pa	Acid plutonic rocks	0.005095	60	0.42
3	pb	Basic plutonic rocks	0.007015	50	0
4	pi	Intermediate plutonic rocks	0.007015	60	0.42
5	py	Pyroclastics	0.0061	46	0
6	sm	Mixed sedimentary rocks	0.012481	60	0.76
7	ss	Siliciclastic sedimentary rocks	0.005341	60	0.36
8	su	Unconsolidated sediments	0.003364	60	0
9	va	Acid volcanic rocks	0.002455	60	0
10	vb	Basic volcanic rocks	0.007015	50	0
11	vi	Intermediate volcanic rocks	0.007015	50	0
12	lo	Loess	0	0	1
13	sc	Carbonate sedimentary rocks	0	0	1
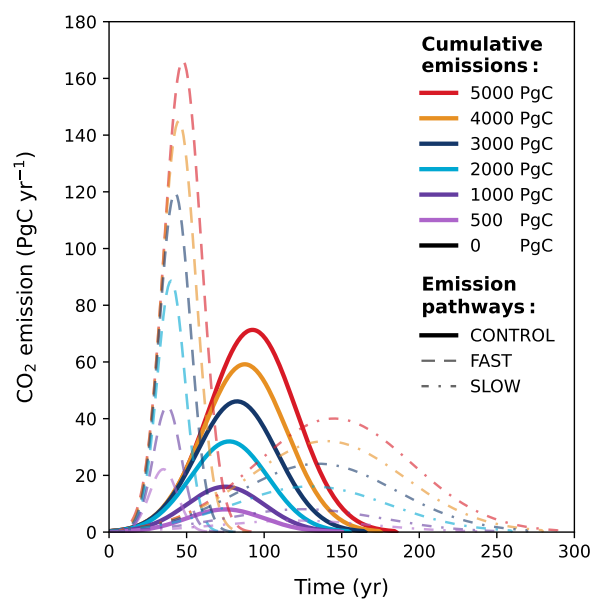
Figure E2. Pathways of emitted carbon as described by 3 different functions. A fourth pathway called 'pulse', not shown here, assumes that all anthropogenic emissions are released on the first timestep of the simulation.
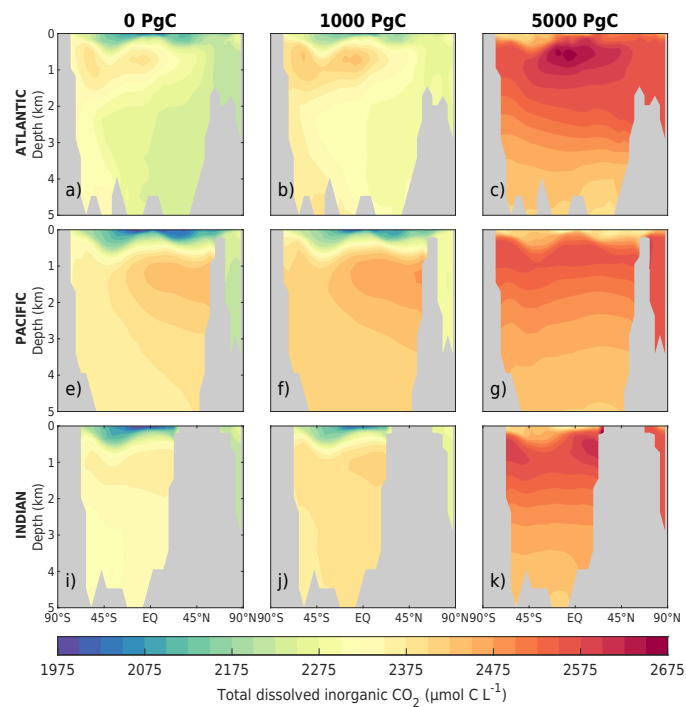
Figure E3. Annual mean dissolved inorganic CO_2 **in 3 oceanic basins at 1** kyr. The top row (a-c) shows the zonal mean cross section of the Atlantic ocean, the middle row (d-f) shows the Pacific ocean, and the bottom row (g-i) shows the Indian ocean. The time slice here is measured from the start of the simulations, meaning it includes the emissions ramp up period.
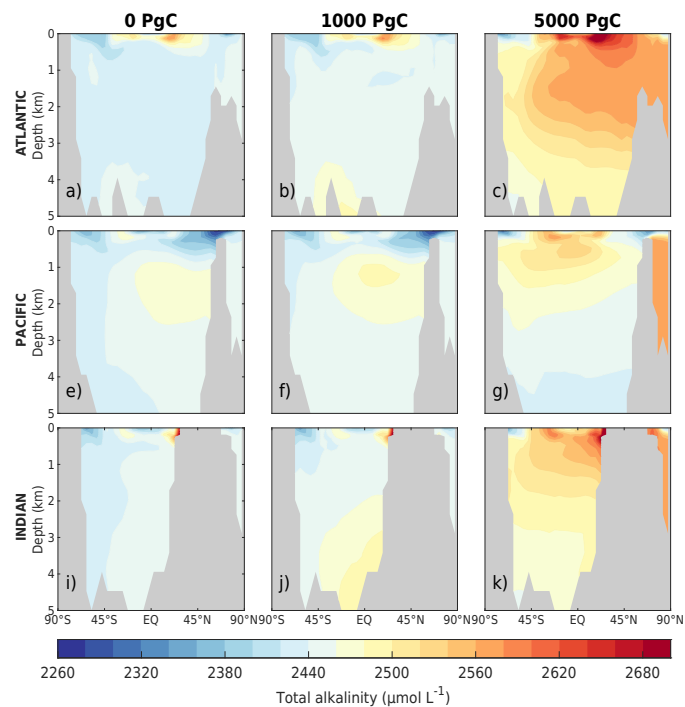
Figure E4. Annual mean alkalinity in 3 oceanic basins at 1 kyr**.** The top row (a-c) shows the zonal mean cross section of the Atlantic ocean, the middle row (d-f) shows the Pacific ocean, and the bottom row (g-i) shows the Indian ocean. The time slice here is measured from the start of the simulations, meaning it includes the emissions ramp up period.
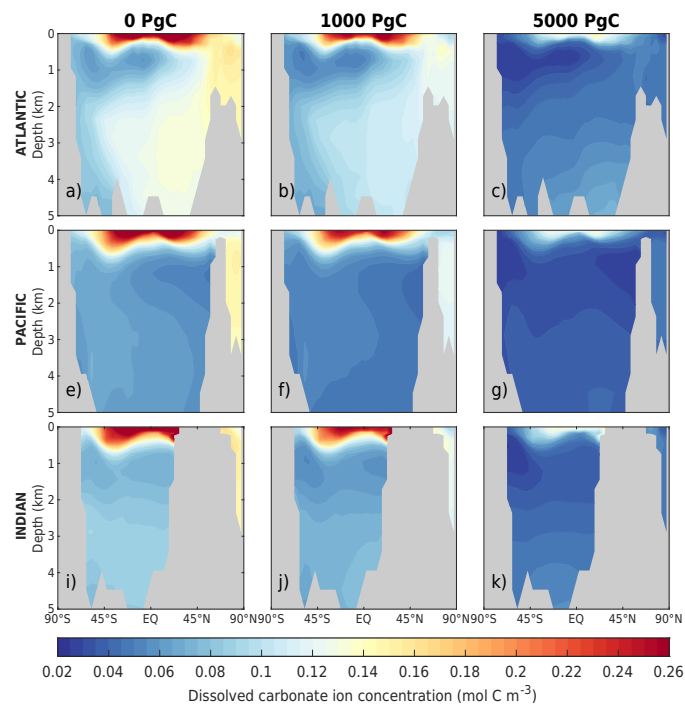
Figure E5. Annual mean dissolved carbonate ion concentration in 3 oceanic basins at 1 kyr**.** The top row (a-c) shows the zonal mean cross section of the Atlantic ocean, the middle row (d-f) shows the Pacific ocean, and the bottom row (g-i) shows the Indian ocean. The time slice here is measured from the start of the simulations, meaning it includes the emissions ramp up period.
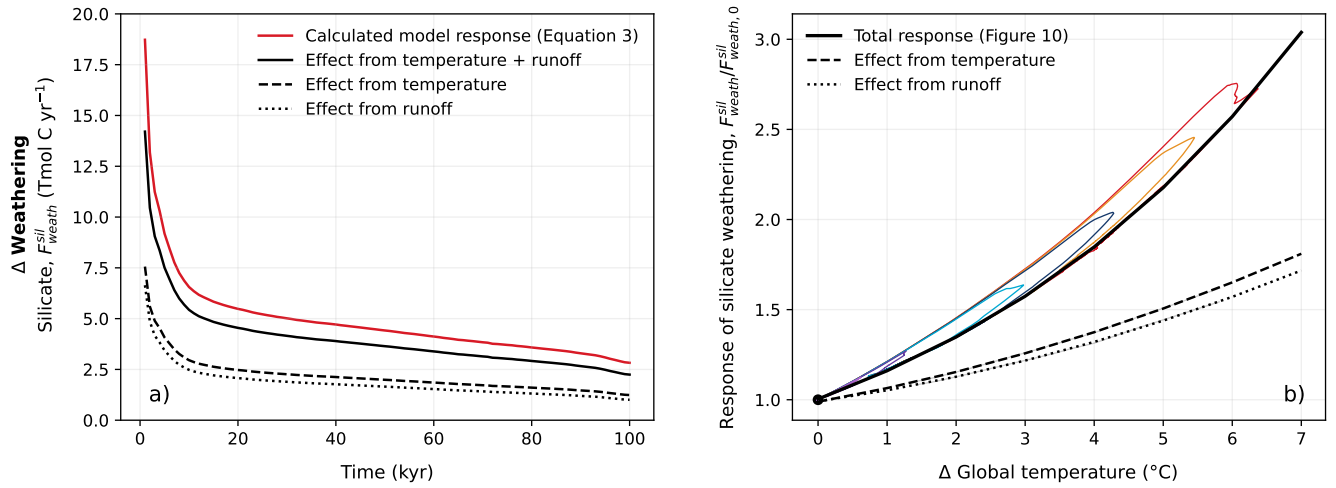
Figure E6. Contribution of temperature and runoff to the silicate weathering response in CLIMBER-X. (a) Change in silicate weathering flux from the pre-industrial (12.3 TmolC yr^{-1}) for the 5000 PgC scenario. The contribution from temperature and runoff was broken down for the 5000 PgC scenario, and do not linearly add to the calculated model response as the weathering relation in Eq. 3 is nonlinear. (b) Response in silicate weathering as a function of global mean temperature. Like Fig. 10, the fit of these trajectories has been plotted above using *Numpy.Polyfit* in Python. The relative contribution of temperature and runoff to the silicate weathering response was determined from the 5000 PgC scenario, i.e., trajectories from (a).
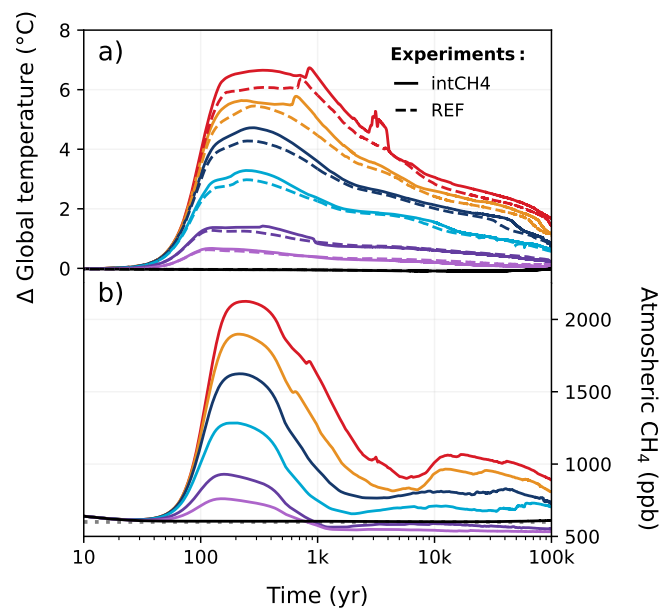
Figure E7. Change in (a) global temperature and (b) atmospheric CH$_4$ **concentration in the intCH4 experiment compared to the REF experiment.** The grey dotted line here in (b) shows the constant CH$_4$ concentration used in the REF experiment (600 pbb). Colours correspond to the cumulative emission scenarios shown in Fig. 2.

Table E2. Fitting parameters used for a multi-exponential decay function describing atmospheric CO_2 concentration in the REF, PULSE, noLAND experiment ensembles. Here, the fraction of emissions (A_i) taken up over the removal timescales (τ_i) associated with ocean invasion (i = 1), $CaCO_3$ reactions (i = 2) and silicate weathering (i = 3) are shown. We highlight that this is the total fraction of emissions removed after peak CO_2 concentrations have been reached. Anthropogenic CO_2 removed during the ramp up of emissions is not considered in this analysis, however, fraction of emissions removed from short-term (sub-centennial timescales) processes can be broadly estimated from $1 - \sum A_i$. While n = 3 was used for consistency across experiments, we acknowledge that a more accurate fit for the PULSE experiments could theoretically be achieved by increasing the number of fitted exponentials (as in Colbourn et al., 2015; Lord et al., 2015b).

Cumulative Emissions, E (PgC)	CO_2 Concentration Peak, CO_2^{max} (ppm)	i =	1	2	3	Fraction Removed, $\sum A_i$	R^2-Value
REF experiment							
500	363	A_i	0.14	0.03	0.05	0.22	0.9989
		τ_i	386	16612	159105		
1000	465	A_i	0.25	0.03	0.11	0.39	0.9992
		τ_i	427	6982	107893		
2000	722	A_i	0.4	0.08	0.14	0.62	0.9983
		τ_i	520	5587	113421		
3000	1047	A_i	0.50	0.11	0.15	0.76	0.9992
		τ_i	626	4128	108592		
4000	1415	A_i	0.51	0.19	0.14	0.84	0.9991
		τ_i	658	3758	117405		
5000	1819	A_i	0.51	0.24	0.13	0.88	0.9992
		τ_i	810	4216	129309		
PULSE experiment							
500	516	A_i	0.14	0.02	0.04	0.20	0.9757
		τ_i	290	18213	151392		
1000	752	A_i	0.22	0.02	0.07	0.30	0.9810
		τ_i	322	5440	107949		
2000	1223	A_i	0.30	0.05	0.08	0.44	0.9897
		τ_i	438	5572	114849		
3000	1695	A_i	0.37	0.08	0.09	0.54	0.9945
		τ_i	562	3930	108888		
4000	2167	A_i	0.38	0.13	0.09	0.60	0.9965
		τ_i	675	3797	116131		
5000	2638	A_i	0.40	0.18	0.09	0.67	0.9980
		τ_i	762	4057	130924		
noLAND experiment							
500	426	A_i	0.25	0.04	0.05	0.34	0.9994
		τ_i	289	17284	112811		
1000	594	A_i	0.38	0 .05	0.1	0.53	0.9996
		τ_i	341	8638	93042		
2000	974	A_i	0.53	0.08	0.1	0.72	0.9996
		τ_i	495	5868	109293		
3000	1381	A_i	0.55	0.14	0.12	0.81	0.9996
		τ_i	602	3733	101937		
4000	1804	A_i	0.55	0.20	0.12	0.87	0.9992
		τ_i	760	3725	111838		
5000	2234	A_i	0.37	0.41	0.10	0.88	0.9993

Data availability. Code and model output can be obtained from https://doi.org/10.5281/zenodo.13933974 (Kaufhold et al., 2024b).

Author contributions. Experimental set-up and design was led by MW and AG. CK conducted the simulations and wrote the manuscript with support from MW, BL, and AG. All authors contributed to the analysis, discussion, and the general quality of the text.

755 *Competing interests.* The authors declare that they have no conflict of interest.

Acknowledgements. CK is funded by the Bundesgesellschaft für Endlagerung through the URS project (research project no. STAFuE-21-4-Klei). MW is supported by the German paleoclimate modelling initiative PalMod (grant nos. 01LP1920B, 01LP1917D, 01LP2305B). BL is supported by the German paleoclimate modelling initiative PalMod (grant nos: 01LP1919B, 01LP2328A). PalMod is part of the Research for Sustainable Development initiative (FONA) funded by the German Federal Ministry of Education and Research (BMBF). The authors
760 gratefully acknowledge the European Regional Development Fund (ERDF), the German Federal Ministry of Education and Research, and the Land Brandenburg for supporting this project by providing resources on the high-performance computer system at the Potsdam Institute for Climate Impact Research. We additionally thank Victor Couplet for helpful discussions and SURFER model output, as well as Richard Zeebe and Peter Köhler for their valuable feedback and suggestions during the peer-review process.

References

Amiotte Suchet, P. and Probst, J.-L.: A global model for present-day atmospheric/soil CO_2 consumption by chemical erosion of Continental Rocks (Gem-CO2), Tellus B, 47, 273–280, https://doi.org/10.1034/j.1600-0889.47.issue1.23.x, 1995.

Amiotte Suchet, P., Probst, J.-L., and Ludwig, W.: Worldwide distribution of continental rock lithology: Implications for the atmospheric/soil CO_2 uptake by continental weathering and alkalinity river transport to the oceans, Global Biogeochemical Cycles, 17, https://doi.org/10.1029/2002GB001891, 2003.

Archer, D.: Fate of fossil fuel CO_2 in geologic time, Journal of Geophysical Research, 110, https://doi.org/10.1029/2004jc002625, 2005.

Archer, D. and Brovkin, V.: The millennial atmospheric lifetime of anthropogenic CO_2, Climatic Change, 90, 283–297, https://doi.org/10.1007/s10584-008-9413-1, 2008.

Archer, D. and Ganopolski, A.: A movable trigger: Fossil fuel CO_2 and the onset of the next glaciation, Geochemistry, Geophysics, Geosystems, 6, https://doi.org/10.1029/2004GC000891, 2005.

Archer, D., Kheshgi, H., and Maier-Reimer, E.: Multiple timescales for neutralization of fossil fuel CO_2, Geophysical Research Letters, 24, 405–408, https://doi.org/10.1029/97gl00168, 1997.

Archer, D., Kheshgi, H., and Maier-Reimer, E.: Dynamics of fossil fuel CO_2 neutralization by marine $CaCO_3$, Global Biogeochemical Cycles, 12, 259–276, https://doi.org/10.1029/98GB00744, 1998.

Archer, D., Eby, M., Brovkin, V., Ridgwell, A., Cao, L., Mikolajewicz, U., Caldeira, K., Matsumoto, K., Munhoven, G., Montenegro, A., and et al.: Atmospheric lifetime of fossil fuel carbon dioxide, Annual Review of Earth and Planetary Sciences, 37, 117–134, https://doi.org/10.1146/annurev.earth.031208.100206, 2009a.

Archer, D., Buffett, B., and Brovkin, V.: Ocean methane hydrates as a slow tipping point in the global carbon cycle, Proceedings of the National Academy of Sciences, 106, 20 596–20 601, https://doi.org/10.1073/pnas.0800885105, 2009b.

Armstrong McKay, D. I., Staal, A., Abrams, J. F., Winkelmann, R., Sakschewski, B., Loriani, S., Fetzer, I., Cornell, S. E., Rockström, J., and Lenton, T. M.: Exceeding 1.5°C global warming could trigger multiple climate tipping points, Science, 377, eabn7950, https://doi.org/10.1126/science.abn7950, 2022.

Beck, J., Bock, M., Schmitt, J., Seth, B., Blunier, T., and Fischer, H.: Bipolar carbon and hydrogen isotope constraints on the Holocene methane budget, Biogeosciences, 15, 7155–7175, https://doi.org/10.5194/bg-15-7155-2018, 2018.

Berger, A. and Loutre, M. F.: An exceptionally long interglacial ahead?, Science, 297, 1287–1288, https://doi.org/10.1126/science.1076120, 2002.

Bluth, G. and Kump, L.: Phanerozoic paleogeology, American Journal of Science, 291, 284–308, https://doi.org/10.2475/ajs.291.3.284, 1991.

Brault, M.-O., Matthews, H. D., and Mysak, L. A.: The importance of terrestrial weathering changes in multimillennial recovery of the global carbon cycle: a two-dimensional perspective, Earth System Dynamics, 8, 455–475, https://doi.org/10.5194/esd-8-455-2017, 2017.

Broecker, W. S., Takahashi, T., Simpson, H. J., and Peng, T. H.: Fate of Fossil Fuel Carbon Dioxide and the Global Carbon Budget, Science, 206, 409–418, https://doi.org/10.1126/science.206.4417.409, 1979.

Brovkin, V., Boysen, L., Arora, V. K., Boisier, J. P., Cadule, P., Chini, L., Claussen, M., Friedlingstein, P., Gayler, V., van den Hurk, B. J., and et al.: Effect of anthropogenic land-use and land-cover changes on climate and land carbon storage in CMIP5 projections for the twenty-first century, Journal of Climate, 26, 6859–6881, https://doi.org/10.1175/jcli-d-12-00623.1, 2013.

Börker, J., Hartmann, J., Amann, T., Romero-Mujalli, G., Moosdorf, N., and Jenkins, C.: Chemical weathering of loess and its contribution to global alkalinity fluxes to the coastal zone during the Last Glacial Maximum, mid-Holocene, and present, Geochemistry, Geophysics, Geosystems, 21, e2020GC008 922, https://doi.org/10.1029/2020GC008922, e2020GC008922 2020GC008922, 2020.

Caldeira, K. and Wickett, M. E.: Ocean model predictions of chemistry changes from carbon dioxide emissions to the atmosphere and ocean, Journal of Geophysical Research: Oceans, 110, https://doi.org/10.1029/2004JC002671, 2005.

Canadell, J., Monteiro, P., Costa, M., Cotrim da Cunha, L., Cox, P., Eliseev, A., Henson, S., Ishii, M., Jaccard, S., Koven, C., Lohila, A., Patra, P., Piao, S., Rogelj, J., Syampungani, S., Zaehle, S., and Zickfeld, K.: Chapter 5: Global carbon and other biogeochemical cycles and feedbacks, in: Climate Change 2021: The Physical Science Basis. Contribution of Working Group I to the Sixth Assessment Report of the Intergovernmental Panel on Climate Change, edited by Masson-Delmotte, V., Zhai, P., Pirani, A., Connors, S., Péan, C., Berger, S., Caud, N., Chen, Y., Goldfarb, L., Gomis, M., Huang, M., Leitzell, K., Lonnoy, E., Matthews, J., Maycock, T., Waterfield, T., Yelekçi, O., Yu, R., and Zhou, B., p. 673–816, Cambridge University Press, Cambridge, United Kingdom and New York, NY, USA, https://doi.org/10.1017/9781009157896.007, 2021.

Cawley, G. C.: On the atmospheric residence time of anthropogenically sourced carbon dioxide, Energy & Fuels, 25, 5503–5513, https://doi.org/10.1021/ef200914u, 2011.

Charbit, S., Paillard, D., and Ramstein, G.: Amount of CO_2 emissions irreversibly leading to the total melting of Greenland, Geophysical Research Letters, 35, https://doi.org/10.1029/2008gl033472, 2008.

Colbourn, G.: Weathering effects on the carbon cycle in an Earth System Model, PhD Thesis, University of East Anglia, Norwich, U. K., available at: https://ueaeprints.uea.ac.uk/id/eprint/34242/, 2011.

Colbourn, G., Ridgwell, A., and Lenton, T. M.: The Rock Geochemical Model (RokGeM) v0.9, Geoscientific Model Development, 6, 1543–1573, https://doi.org/10.5194/gmd-6-1543-2013, 2013.

Colbourn, G., Ridgwell, A., and Lenton, T. M.: The time scale of the silicate weathering negative feedback on atmospheric CO_2, Global Biogeochemical Cycles, 29, 583–596, https://doi.org/10.1002/2014GB005054, 2015.

Couplet, V., Martínez Montero, M., and Crucifix, M.: SURFER v3.0: a fast model with ice sheet tipping points and carbon cycle feedbacks for short and long-term climate scenarios, EGUsphere, 2024, 1–77, https://doi.org/10.5194/egusphere-2024-2279, (in review), 2024.

Duque-Villegas, M., Claussen, M., Brovkin, V., and Kleinen, T.: Effects of orbital forcing, greenhouse gases and ice sheets on Saharan greening in past and future multi-millennia, Climate of the Past, 18, 1897–1914, https://doi.org/10.5194/cp-18-1897-2022, 2022.

Eby, M., Zickfeld, K., Montenegro, A., Archer, D., Meissner, K. J., and Weaver, A. J.: Lifetime of anthropogenic climate change: Millennial time scales of potential CO_2 and surface temperature perturbations, Journal of Climate, 22, 2501–2511, https://doi.org/10.1175/2008jcli2554.1, 2009.

Eby, M., Weaver, A. J., Alexander, K., Zickfeld, K., Abe-Ouchi, A., Cimatoribus, A. A., Crespin, E., Drijfhout, S. S., Edwards, N. R., Eliseev, A. V., and et al.: Historical and idealized climate model experiments: An intercomparison of Earth system models of intermediate complexity, Climate of the Past, 9, 1111–1140, https://doi.org/10.5194/cp-9-1111-2013, 2013.

Edwards, N. R. and Marsh, R.: Uncertainties due to transport-parameter sensitivity in an efficient 3-D ocean-climate model, Climate Dynamics, 24, 415–433, https://doi.org/10.1007/s00382-004-0508-8, 2005.

Edwards, N. R., Willmott, A. J., and Killworth, P. D.: On the role of topography and wind stress on the stability of the thermohaline circulation, Journal of Physical Oceanography, 28, 756–778, https://doi.org/10.1175/1520-0485(1998)028<0756:OTROTA>2.0.CO;2, 1998.

Egleston, E. S., Sabine, C. L., and Morel, F. M. M.: Revelle revisited: Buffer factors that quantify the response of ocean chemistry to changes in DIC and alkalinity, Global Biogeochemical Cycles, 24, https://doi.org/10.1029/2008GB003407, 2010.

Friedlingstein, P., O'Sullivan, M., Jones, M. W., Andrew, R. M., Bakker, D. C. E., Hauck, J., Landschützer, P., Le Quéré, C., Luijkx, I. T., Peters, G. P., Peters, W., Pongratz, J., Schwingshackl, C., Sitch, S., Canadell, J. G., Ciais, P., Jackson, R. B., Alin, S. R., Anthoni, P., Barbero, L., Bates, N. R., Becker, M., Bellouin, N., Decharme, B., Bopp, L., Brasika, I. B. M., Cadule, P., Chamberlain, M. A., Chandra, N., Chau, T.-T.-T., Chevallier, F., Chini, L. P., Cronin, M., Dou, X., Enyo, K., Evans, W., Falk, S., Feely, R. A., Feng, L., Ford, D. J., Gasser, T., Ghattas, J., Gkritzalis, T., Grassi, G., Gregor, L., Gruber, N., Gürses, O., Harris, I., Hefner, M., Heinke, J., Houghton, R. A., Hurtt, G. C., Iida, Y., Ilyina, T., Jacobson, A. R., Jain, A., Jarníková, T., Jersild, A., Jiang, F., Jin, Z., Joos, F., Kato, E., Keeling, R. F., Kennedy, D., Klein Goldewijk, K., Knauer, J., Korsbakken, J. I., Körtzinger, A., Lan, X., Lefèvre, N., Li, H., Liu, J., Liu, Z., Ma, L., Marland, G., Mayot, N., McGuire, P. C., McKinley, G. A., Meyer, G., Morgan, E. J., Munro, D. R., Nakaoka, S.-I., Niwa, Y., O'Brien, K. M., Olsen, A., Omar, A. M., Ono, T., Paulsen, M., Pierrot, D., Pocock, K., Poulter, B., Powis, C. M., Rehder, G., Resplandy, L., Robertson, E., Rödenbeck, C., Rosan, T. M., Schwinger, J., Séférian, R., Smallman, T. L., Smith, S. M., Sospedra-Alfonso, R., Sun, Q., Sutton, A. J., Sweeney, C., Takao, S., Tans, P. P., Tian, H., Tilbrook, B., Tsujino, H., Tubiello, F., van der Werf, G. R., van Ooijen, E., Wanninkhof, R., Watanabe, M., Wimart-Rousseau, C., Yang, D., Yang, X., Yuan, W., Yue, X., Zaehle, S., Zeng, J., and Zheng, B.: Global Carbon Budget 2023, Earth System Science Data, 15, 5301–5369, https://doi.org/10.5194/essd-15-5301-2023, 2023.

Gaillardet, J., Dupré, B., Louvat, P., and Allègre, C.: Global silicate weathering and CO_2 consumption rates deduced from the chemistry of large rivers, Chemical Geology, 159, 3–30, https://doi.org/10.1016/S0009-2541(99)00031-5, 1999.

Ganopolski, A., Winkelmann, R., and Schellnhuber, H. J.: Critical insolation-CO_2 relation for diagnosing past and future glacial inception, Nature, 534, https://doi.org/10.1038/nature18452, 2016.

Goddéris, Y., Donnadieu, Y., Tombozafy, M., and Dessert, C.: Shield effect on continental weathering: Implication for climatic evolution of the Earth at the geological timescale, Geoderma, 145, 439–448, https://doi.org/10.1016/j.geoderma.2008.01.020, modelling Pedogenesis, 2008.

Goodwin, P. and Ridgwell, A.: Ocean-atmosphere partitioning of anthropogenic carbon dioxide on multimillennial timescales, Global Biogeochemical Cycles, 24, https://doi.org/10.1029/2008GB003449, 2010.

Hartmann, J.: Bicarbonate-fluxes and CO_2-consumption by chemical weathering on the Japanese Archipelago — Application of a multi-lithological model framework, Chemical Geology, 265, 237–271, https://doi.org/10.1016/j.chemgeo.2009.03.024, 2009a.

Hartmann, J. and Moosdorf, N.: The new global lithological map database GLiM: A representation of rock properties at the Earth surface, Geochemistry, Geophysics, Geosystems, 13, https://doi.org/10.1029/2012GC004370, 2012.

Hartmann, J., Jansen, N., Dürr, H. H., Kempe, S., and Köhler, P.: Global CO_2-consumption by chemical weathering: What is the contribution of highly active weathering regions?, Global and Planetary Change, 69, 185–194, https://doi.org/10.1016/j.gloplacha.2009.07.007, 2009b.

Hartmann, J., Moosdorf, N., Lauerwald, R., Hinderer, M., and West, A. J.: Global chemical weathering and associated P-release — The role of lithology, temperature and soil properties, Chemical Geology, 363, 145–163, https://doi.org/10.1016/j.chemgeo.2013.10.025, 2014.

Heinze, C. and Maier-Reimer, E.: The Hamburg oceanic carbon cycle circulation model version "HAMOCC2s" for long time integrations, Tech. Rep. 20, Deutsches Klimarechenzentrum, Modellbetreuungsgruppe, Hamburg, Germany, TRN DE00G1064, ISSN 0940-9327, 1999.

Herrero, C., García-Olivares, A., and Pelegrí, J. L.: Impact of anthropogenic CO_2 on the next glacial cycle, Climatic Change, 122, 283–298, https://doi.org/10.1007/s10584-013-1012-0, 2013.

Herrington, T. and Zickfeld, K.: Path independence of climate and carbon cycle response over a broad range of cumulative carbon emissions, Earth System Dynamics, 5, 409–422, https://doi.org/10.5194/esd-5-409-2014, 2014.

Höning, D., Willeit, M., and Ganopolski, A.: Reversibility of Greenland ice sheet mass loss under artificial carbon dioxide removal scenarios, Environmental Research Letters, http://iopscience.iop.org/article/10.1088/1748-9326/ad2129, 2024.

Höning, D., Willeit, M., Calov, R., Klemann, V., Bagge, M., and Ganopolski, A.: Multistability and transient response of the Greenland ice sheet to anthropogenic CO_2 emissions, Geophysical Research Letters, 50, e2022GL101 827, https://doi.org/10.1029/2022GL101827, 2023.

Ilyina, T., Six, K. D., Segschneider, J., Maier-Reimer, E., Li, H., and Núñez-Riboni, I.: The global ocean biogeochemistry model HAMOCC: Model architecture and performance as component of the MPI-Earth system model in different CMIP5 experimental realizations, Journal of Advances in Modeling Earth Systems, https://doi.org/10.1002/jame.20017, 2013.

Jeltsch-Thömmes, A. and Joos, F.: Modeling the evolution of pulse-like perturbations in atmospheric carbon and carbon isotopes: the role of weathering–sedimentation imbalances, Climate of the Past, 16, 423–451, https://doi.org/10.5194/cp-16-423-2020, 2020.

Jiang, L.-Q., Carter, B. R., Feely, R. A., Lauvset, S. K., and Olsen, A.: Surface ocean pH and buffer capacity: past, present and future, Scientific Reports, 9, 18 624, https://doi.org/10.1038/s41598-019-55039-4, 2019.

Jones, C., Robertson, E., Arora, V., Friedlingstein, P., Shevliakova, E., Bopp, L., Brovkin, V., Hajima, T., Kato, E., Kawamiya, M., and et al.: Twenty-first-century compatible CO_2 emissions and Airborne Fraction simulated by CMIP5 Earth system models under four representative concentration pathways, Journal of Climate, 26, 4398–4413, https://doi.org/10.1175/jcli-d-12-00554.1, 2013.

Joos, F., Roth, R., Fuglestvedt, J. S., Peters, G. P., Enting, I. G., von Bloh, W., Brovkin, V., Burke, E. J., Eby, M., Edwards, N. R., and et al.: Carbon dioxide and climate impulse response functions for the computation of greenhouse gas metrics: A multi-model analysis, Atmospheric Chemistry and Physics, 13, 2793–2825, https://doi.org/10.5194/acp-13-2793-2013, 2013.

Kaufhold, C., Willeit, M., Talento, S., Ganopolski, A., and Rockström, J.: Interplay between climate and carbon cycle feedbacks could substantially enhance future warming, Environmental Research Letters, (in review), 2024a.

Kaufhold, C., Willeit, M., Liu, B., and Ganopolski, A.: Data set for the study "Assessing the lifetime of anthropogenic CO_2 and its sensitivity to different carbon cycle processes", https://doi.org/10.5281/zenodo.13955664, 2024b.

Kurgyis, K., Achtziger-Zupančič, P., Bjorge, M., Boxberg, M. S., Broggi, M., Buchwald, J., Ernst, O. G., Flügge, J., Ganopolski, A., Graf, T., Kortenbruck, P., Kowalski, J., Kreye, P., Kukla, P., Mayr, S., Miro, S., Nagel, T., Nowak, W., Oladyshkin, S., Renz, A., Rienäcker-Burschil, J., Röhlig, K.-J., Sträter, O., Thiedau, J., Wagner, F., Wellmann, F., Wengler, M., Wolf, J., and Rühaak, W.: Uncertainties and robustness with regard to the safety of a repository for high-level radioactive waste: Introduction of a research initiative, Environmental Earth Sciences, 83, 82, https://doi.org/10.1007/s12665-023-11346-8, 2024.

Köhler, P.: Anthropogenic CO_2 of High Emission Scenario Compensated After 3500 Years of Ocean Alkalinization With an Annually Constant Dissolution of 5 Pg of Olivine, Frontiers in Climate, 2, https://doi.org/10.3389/fclim.2020.575744, 2020.

Lal, R.: Carbon sequestration, Philosophical Transactions of the Royal Society B: Biological Sciences, 363, 815–830, https://doi.org/10.1098/rstb.2007.2185, 2008.

Laufkötter, C., Vogt, M., Gruber, N., Aita-Noguchi, M., Aumont, O., Bopp, L., Buitenhuis, E., Doney, S. C., Dunne, J., Hashioka, T., and et al.: Drivers and uncertainties of future global marine primary production in Marine Ecosystem Models, Biogeosciences, 12, 6955–6984, https://doi.org/10.5194/bg-12-6955-2015, 2015.

Lenton, T. M. and Britton, C.: Enhanced carbonate and silicate weathering accelerates recovery from fossil fuel CO_2 perturbations, Global Biogeochemical Cycles, 20, https://doi.org/10.1029/2005gb002678, 2006.

Lenton, T. M., Held, H., Kriegler, E., Hall, J. W., Lucht, W., Rahmstorf, S., and Schellnhuber, H. J.: Tipping elements in the Earth's climate system, Proceedings of the National Academy of Sciences, 105, 1786–1793, https://doi.org/10.1073/pnas.0705414105, 2008.

Lindborg, T., Thorne, M., Andersson, E., Becker, J., Brandefelt, J., Cabianca, T., Gunia, M., Ikonen, A., Johansson, E., Kangasniemi, V., Kautsky, U., Kirchner, G., Klos, R., Kowe, R., Kontula, A., Kupiainen, P., Lahdenperä, A.-M., Lord, N. S., Lunt, D. J., Näslund, J.-O., Nordén, M., Norris, S., Pérez-Sánchez, D., Proverbio, A., Riekki, K., Rübel, A., Sweeck, L., Walke, R., Xu, S., Smith, G., and Pröhl, G.: Climate change and landscape development in post-closure safety assessment of solid radioactive waste disposal: Results of an initiative of the IAEA, Journal of Environmental Radioactivity, 183, 41–53, https://doi.org/10.1016/j.jenvrad.2017.12.006, 2018.

Lord, N. S., Ridgwell, A., Thorne, M. C., and Lunt, D. J.: The "long tail" of anthropogenic CO_2 decline in the atmosphere and its consequences for post-closure performance assessments for disposal of radioactive wastes, Mineralogical Magazine, 79, 1613–1623, https://doi.org/10.1180/minmag.2015.079.6.37, 2015a.

Lord, N. S., Ridgwell, A., Thorne, M. C., and Lunt, D. J.: An impulse response function for the "long tail" of excess atmospheric CO_2 in an Earth system model, Global Biogeochemical Cycles, 30, 2–17, https://doi.org/10.1002/2014gb005074, 2015b.

Maffre, P., Chiang, J. C. H., and Swanson-Hysell, N. L.: The effect of the Pliocene temperature pattern on silicate weathering and Pliocene–Pleistocene cooling, Climate of the Past, 19, 1461–1479, https://doi.org/10.5194/cp-19-1461-2023, 2023.

Maher, K. and Chamberlain, C. P.: Hydrologic Regulation of Chemical Weathering and the Geologic Carbon Cycle, Science, 343, 1502–1504, https://doi.org/10.1126/science.1250770, 2014.

Maier-Reimer, E. and Hasselmann, K.: Transport and storage of CO_2 in the ocean – an inorganic ocean-circulation carbon cycle model, Climate Dynamics, 2, 63–90, https://doi.org/10.1007/bf01054491, 1987.

Matthews, H. D., Gillett, N. P., Stott, P. A., and Zickfeld, K.: The proportionality of global warming to cumulative carbon emissions, Nature, 459, 829–832, https://doi.org/10.1038/nature08047, 2009.

Mauritsen, T., Bader, J., Becker, T., Behrens, J., Bittner, M., Brokopf, R., Brovkin, V., Claussen, M., Crueger, T., Esch, M., Fast, I., Fiedler, S., Fläschner, D., Gayler, V., Giorgetta, M., Goll, D. S., Haak, H., Hagemann, S., Hedemann, C., Hohenegger, C., Ilyina, T., Jahns, T., Jimenéz-de-la Cuesta, D., Jungclaus, J., Kleinen, T., Kloster, S., Kracher, D., Kinne, S., Kleberg, D., Lasslop, G., Kornblueh, L., Marotzke, J., Matei, D., Meraner, K., Mikolajewicz, U., Modali, K., Möbis, B., Müller, W. A., Nabel, J. E. M. S., Nam, C. C. W., Notz, D., Nyawira, S.-S., Paulsen, H., Peters, K., Pincus, R., Pohlmann, H., Pongratz, J., Popp, M., Raddatz, T. J., Rast, S., Redler, R., Reick, C. H., Rohrschneider, T., Schemann, V., Schmidt, H., Schnur, R., Schulzweida, U., Six, K. D., Stein, L., Stemmler, I., Stevens, B., von Storch, J.-S., Tian, F., Voigt, A., Vrese, P., Wieners, K.-H., Wilkenskjeld, S., Winkler, A., and Roeckner, E.: Developments in the MPI-M Earth system model version 1.2 (MPI-ESM1.2) and its response to increasing CO_2, Journal of Advances in Modeling Earth Systems, 11, 998–1038, https://doi.org/10.1029/2018MS001400, 2019.

McGlade, C. and Ekins, P.: The geographical distribution of fossil fuels unused when limiting global warming to 2 °C, Nature, 517, 187–190, https://doi.org/10.1038/nature14016, 2015.

Meissner, K. J., McNeil, B. I., Eby, M., and Wiebe, E. C.: The importance of the terrestrial weathering feedback for multimillennial coral reef habitat recovery, Global Biogeochemical Cycles, 26, https://doi.org/10.1029/2011GB004098, 2012.

Meybeck, M.: Global chemical weathering of surficial rocks estimated from river dissolved loads, American Journal of Science, 287, 401–428, https://doi.org/10.2475/ajs.287.5.401, 1987.

Middelburg, J. J., Soetaert, K., and Hagens, M.: Ocean alkalinity, buffering and biogeochemical processes, Reviews of Geophysics, 58, e2019RG000 681, https://doi.org/10.1029/2019RG000681, e2019RG000681 2019RG000681, 2020.

Mikolajewicz, U., Gröger, M., Maier-Reimer, E., Schurgers, G., Vizcaíno, M., and Winguth, A. M.: Long-term effects of anthropogenic CO_2 emissions simulated with a complex Earth system model, Climate Dynamics, 28, 599–633, https://doi.org/10.1007/s00382-006-0204-y, 2006.

950 Mitchell, L., Brook, E., Lee, J. E., Buizert, C., and Sowers, T.: Constraints on the late Holocene anthropogenic contribution to the atmospheric methane budget, Science, 342, 964–966, https://doi.org/10.1126/science.1238920, 2013.

Montenegro, A., Brovkin, V., Eby, M., Archer, D., and Weaver, A. J.: Long term fate of anthropogenic carbon, Geophysical Research Letters, 34, https://doi.org/10.1029/2007gl030905, 2007.

Mora, C., Wei, C.-L., Rollo, A., Amaro, T., Baco, A. R., Billett, D., Bopp, L., Chen, Q., Collier, M., Danovaro, R., and
955 et al.: Biotic and human vulnerability to projected changes in ocean biogeochemistry over the 21st century, PLoS Biology, 11, https://doi.org/10.1371/journal.pbio.1001682, 2013.

Munhoven, G.: Glacial–interglacial changes of continental weathering: estimates of the related CO_2 and HCO_3^- flux variations and their uncertainties, Global and Planetary Change, 33, 155–176, https://doi.org/10.1016/S0921-8181(02)00068-1, in: The global carbon cycle and its changes over glacial-interglacial cycles, 2002.

960 Munhoven, G. and François, L. M.: Glacial-interglacial changes in continental weathering: Possible implications for atmospheric CO_2, in: Carbon cycling in the glacial ocean: Constraints on the ocean's role in global change, edited by Zahn, R., Pedersen, T. F., Kaminski, M. A., and Labeyrie, L., pp. 39–58, Springer Berlin Heidelberg, Berlin, Heidelberg, 1994.

Norby, R. J., Warren, J. M., Iversen, C. M., Medlyn, B. E., and McMurtrie, R. E.: CO_2 enhancement of forest productivity constrained by limited nitrogen availability, Proceedings of the National Academy of Sciences, 107, 19 368–19 373,
965 https://doi.org/10.1073/pnas.1006463107, 2010.

Nugent, K. A. and Matthews, H. D.: Drivers of Future Northern Latitude Runoff Change, Atmosphere-Ocean, 50, 197–206, https://doi.org/10.1080/07055900.2012.658505, 2012.

Näslund, J.-O., Brandefelt, J., and Liljedahl, L. C.: Climate considerations in long-term safety assessments for nuclear waste repositories, AMBIO, 42, 393–401, https://doi.org/10.1007/s13280-013-0406-6, 2013.

970 Revelle, R.: Warming of the Earth, in: Second Supplemental Appropriation Bill, 1956: Hearings Before Subcommittees of the Committee on Appropriations, House of Representatives, Eighty-fourth Congress, Second Session, p. 473, U.S. Government Printing Office, United States. Congress. House. Committee on Appropriations and Rabaut, L.C. and United States. Congress House and United States. Congress. House. Committee on Appropriations. Subcommittee on District of Columbia Appropriations, 1956.

Revelle, R. and Suess, H. E.: Carbon Dioxide Exchange Between Atmosphere and Ocean and the Question of an Increase of Atmospheric
975 CO_2 during the Past Decades, Tellus, 9, 18–27, https://doi.org/10.1111/j.2153-3490.1957.tb01849.x, 1957.

Revelle, R., Broecker, W., Craig, H., Kneeling, C. D., and Smagorinsky, J.: Restoring the Quality of Our Environment: Report, Report of the Environmental Pollution Panel President's Science Advisory Committee, United States. President's Science Advisory Committee. Environmental Pollution Panel, White House, 1965.

Ricke, K. L. and Caldeira, K.: Maximum warming occurs about one decade after a carbon dioxide emission, Environmental Research Letters,
980 9, 124 002, https://doi.org/10.1088/1748-9326/9/12/124002, 2014.

Ridgwell, A. and Hargreaves, J. C.: Regulation of atmospheric CO_2 by deep-sea sediments in an Earth system model, Global Biogeochemical Cycles, 21, https://doi.org/10.1029/2006gb002764, 2007.

Sapart, C. J., Monteil, G., Prokopiou, M., van de Wal, R. S. W., Kaplan, J. O., Sperlich, P., Krumhardt, K. M., van der Veen, C., Houweling, S., Krol, M. C., Blunier, T., Sowers, T., Martinerie, P., Witrant, E., Dahl-Jensen, D., and Röckmann, T.: Natural and anthropogenic variations
985 in methane sources during the past two millennia, Nature, 490, 85–88, https://doi.org/10.1038/nature11461, 2012.

Sarmiento, J. L. and Gruber, N.: Ocean Biogeochemical Dynamics, Princeton University Press, http://www.jstor.org/stable/j.ctt3fgxqx, 2006.

Shaffer, G.: Long-term effectiveness and consequences of carbon dioxide sequestration, Nature Geoscience, 3, 464–467, https://doi.org/10.1038/ngeo896, 2010.

Shaffer, G., Olsen, S. M., and Pedersen, J. O.: Long-term ocean oxygen depletion in response to carbon dioxide emissions from fossil fuels, Nature Geoscience, 2, 105–109, https://doi.org/10.1038/ngeo420, 2009.

Sundquist, E. T.: Steady- and non-steady-state carbonate-silicate controls on atmospheric CO_2, Quaternary Science Reviews, 10, 283–296, https://doi.org/10.1016/0277-3791(91)90026-Q, 1991.

Talento, S. and Ganopolski, A.: Reduced-complexity model for the impact of anthropogenic CO_2 emissions on future glacial cycles, Earth System Dynamics, 12, 1275–1293, https://doi.org/10.5194/esd-12-1275-2021, 2021.

Talento, S., Willeit, M., and Ganopolski, A.: New estimation of critical insolation–CO_2 relationship for triggering glacial inception, Climate of the Past, 20, 1349–1364, https://doi.org/10.5194/cp-20-1349-2024, 2024.

Terhaar, J., Frölicher, T. L., and Joos, F.: Observation-constrained estimates of the global ocean carbon sink from Earth system models, Biogeosciences, 19, 4431–4457, https://doi.org/10.5194/bg-19-4431-2022, 2022.

Turner, J. P., Berry, T. W., Bowman, M. J., and Chapman, N. A.: Role of the geosphere in deep nuclear waste disposal – An England and Wales perspective, Earth-Science Reviews, 242, 104 445, https://doi.org/10.1016/j.earscirev.2023.104445, 2023.

Tyrrell, T.: Calcium carbonate cycling in future oceans and its influence on future climates, Journal of Plankton Research, 30, 141–156, https://doi.org/10.1093/plankt/fbm105, 2007b.

Tyrrell, T., Shepherd, J. G., and Castle, S.: The long-term legacy of fossil fuels, Tellus B: Chemical and Physical Meteorology, 59, 664, https://doi.org/10.1111/j.1600-0889.2007.00290.x, 2007a.

Uchikawa, J. and Zeebe, R. E.: Influence of terrestrial weathering on ocean acidification and the next glacial inception, Geophysical Research Letters, 35, https://doi.org/10.1029/2008gl035963, 2008.

Vakilifard, N., Williams, R. G., Holden, P. B., Turner, K., Edwards, N. R., and Beerling, D. J.: Impact of negative and positive CO_2 emissions on global warming metrics using an ensemble of Earth system model simulations, Biogeosciences, 19, 4249–4265, https://doi.org/10.5194/bg-19-4249-2022, 2022.

Voulgarakis, A., Naik, V., Lamarque, J.-F., Shindell, D. T., Young, P. J., Prather, M. J., Wild, O., Field, R. D., Bergmann, D., Cameron-Smith, P., Cionni, I., Collins, W. J., Dalsøren, S. B., Doherty, R. M., Eyring, V., Faluvegi, G., Folberth, G. A., Horowitz, L. W., Josse, B., MacKenzie, I. A., Nagashima, T., Plummer, D. A., Righi, M., Rumbold, S. T., Stevenson, D. S., Strode, S. A., Sudo, K., Szopa, S., and Zeng, G.: Analysis of present day and future OH and methane lifetime in the ACCMIP simulations, Atmospheric Chemistry and Physics, 13, 2563–2587, https://doi.org/10.5194/acp-13-2563-2013, 2013.

Wadham, J. L., Hawkings, J. R., Tarasov, L., Gregoire, L. J., Spencer, R. G. M., Gutjahr, M., Ridgwell, A., and Kohfeld, K. E.: Ice sheets matter for the global carbon cycle, Nature Communications, 10, 3567, https://doi.org/10.1038/s41467-019-11394-4, 2019.

Walker, J. C. and Kasting, J. F.: Effects of fuel and forest conservation on future levels of atmospheric carbon dioxide, Palaeogeography, Palaeoclimatology, Palaeoecology, 97, 151–189, https://doi.org/10.1016/0031-0182(92)90207-l, 1992.

Willeit, M. and Ganopolski, A.: PALADYN v1.0, a comprehensive land surface–vegetation–carbon cycle model of intermediate complexity, Geoscientific Model Development, 9, 3817–3857, https://doi.org/10.5194/gmd-9-3817-2016, 2016.

Willeit, M., Ganopolski, A., Robinson, A., and Edwards, N. R.: The Earth system model CLIMBER-X v1.0 – Part 1: Climate model description and validation, Geoscientific Model Development, 15, 5905–5948, https://doi.org/10.5194/gmd-15-5905-2022, 2022.

Willeit, M., Ilyina, T., Liu, B., Heinze, C., Perrette, M., Heinemann, M., Dalmonech, D., Brovkin, V., Munhoven, G., Börker, J., Hartmann, J., Romero-Mujalli, G., and Ganopolski, A.: The Earth system model CLIMBER-X v1.0 – Part 2: The global carbon cycle, Geoscientific Model Development, 16, 3501–3534, https://doi.org/10.5194/gmd-16-3501-2023, 2023.

Willeit, M., Calov, R., Talento, S., Greve, R., Bernales, J., Klemann, V., Bagge, M., and Ganopolski, A.: Glacial inception through rapid ice area increase driven by albedo and vegetation feedbacks, Climate of the Past, 20, 597–623, https://doi.org/10.5194/cp-20-597-2024, 2024.

Wunderling, N., von der Heydt, A. S., Aksenov, Y., Barker, S., Bastiaansen, R., Brovkin, V., Brunetti, M., Couplet, V., Kleinen, T., Lear, C. H., Lohmann, J., Roman-Cuesta, R. M., Sinet, S., Swingedouw, D., Winkelmann, R., Anand, P., Barichivich, J., Bathiany, S., Baudena, M., Bruun, J. T., Chiessi, C. M., Coxall, H. K., Docquier, D., Donges, J. F., Falkena, S. K. J., Klose, A. K., Obura, D., Rocha, J., Rynders, S., Steinert, N. J., and Willeit, M.: Climate tipping point interactions and cascades: A review, Earth System Dynamics, 15, 41–74, https://doi.org/10.5194/esd-15-41-2024, 2024.

Zickfeld, K. and Herrington, T.: The time lag between a carbon dioxide emission and maximum warming increases with the size of the emission, Environmental Research Letters, 10, 031 001, https://doi.org/10.1088/1748-9326/10/3/031001, 2015.

Zickfeld, K., Arora, V. K., and Gillett, N. P.: Is the climate response to CO_2 emissions path dependent?, Geophysical Research Letters, 39, https://doi.org/10.1029/2011gl050205, 2012.

Zickfeld, K., Eby, M., Weaver, A. J., Alexander, K., Crespin, E., Edwards, N. R., Eliseev, A. V., Feulner, G., Fichefet, T., Forest, C. E., and et al.: Long-term climate change commitment and reversibility: An EMIC intercomparison, Journal of Climate, 26, 5782–5809, https://doi.org/10.1175/jcli-d-12-00584.1, 2013.